IOWA STATE UNIVERSITY
Digital Repository

Retrospective Theses and Dissertations

Iowa State University Capstones, Theses and Dissertations

1994

Design and modeling of graded bandgap amorphous silicon-germanium solar cells fabricated by plasma enhanced chemical vapor deposition

Greg Charles Baldwin
Iowa State University

Follow this and additional works at: https://lib.dr.iastate.edu/rtd

Part of the Electrical and Electronics Commons, and the Materials Science and Engineering Commons

Recommended Citation

Baldwin, Greg Charles, "Design and modeling of graded bandgap amorphous silicon-germanium solar cells fabricated by plasma enhanced chemical vapor deposition " (1994). *Retrospective Theses and Dissertations*. 10675.
https://lib.dr.iastate.edu/rtd/10675

This Dissertation is brought to you for free and open access by the Iowa State University Capstones, Theses and Dissertations at Iowa State University Digital Repository. It has been accepted for inclusion in Retrospective Theses and Dissertations by an authorized administrator of Iowa State University Digital Repository. For more information, please contact digirep@iastate.edu.

المنارة للاستشارات

www.manaraa.com

95

03528

U·M·I
MICROFILMED 1994

INFORMATION TO USERS

This manuscript has been reproduced from the microfilm master. UMI films the text directly from the original or copy submitted. Thus, some thesis and dissertation copies are in typewriter face, while others may be from any type of computer printer.

The quality of this reproduction is dependent upon the quality of the copy submitted. Broken or indistinct print, colored or poor quality illustrations and photographs, print bleedthrough, substandard margins, and improper alignment can adversely affect reproduction.

In the unlikely event that the author did not send UMI a complete manuscript and there are missing pages, these will be noted. Also, if unauthorized copyright material had to be removed, a note will indicate the deletion.

Oversize materials (e.g., maps, drawings, charts) are reproduced by sectioning the original, beginning at the upper left-hand corner and continuing from left to right in equal sections with small overlaps. Each original is also photographed in one exposure and is included in reduced form at the back of the book.

Photographs included in the original manuscript have been reproduced xerographically in this copy. Higher quality 6" x 9" black and white photographic prints are available for any photographs or illustrations appearing in this copy for an additional charge. Contact UMI directly to order.

U·M·I

University Microfilms International
A Bell & Howell Information Company
300 North Zeeb Road, Ann Arbor, MI 48106-1346 USA
313/761-4700 800/521-0600

Order Number 9503528

Design and modeling of graded bandgap amorphous silicon-germanium solar cells fabricated by plasma enhanced chemical vapor deposition

Baldwin, Greg Charles, Ph.D.

Iowa State University, 1994

U·M·I
300 N. Zeeb Rd.
Ann Arbor, MI 48106

Design and modeling of graded bandgap amorphous silicon-germanium solar cells

fabricated by plasma enhanced chemical vapor deposition

by

Greg Charles Baldwin

A Dissertation Submitted to the

Graduate Faculty in Partial Fulfillment of the

Requirements for the Degree of

DOCTOR OF PHILOSOPHY

Department: Electrical Engineering and Computer Engineering
Major: Electrical Engineering (Microelectronics)

Approved:

Signature was redacted for privacy.

In Charge of Major Work

Signature was redacted for privacy.

For the Major Department

Signature was redacted for privacy.

For the Graduate College

Iowa State University
Ames, Iowa

1994

TABLE OF CONTENTS

Page

ABSTRACT iv

I. INTRODUCTION 1

A. Amorphous Silicon Photovoltaics 1

B. Overview of a-Si:H Research 3

C. Properties of a-Si:H 7

1. Continuous Random Network 7

2. Metastability 12

3. Electronic Structure and Transport 13

D. A-Si:H Growth 17

E. Device Design 19

F. Scope of Research 22

II. SAMPLE PREPARATION 25

A. Deposition System 25

B. PECVD Processing 29

C. Metallization 36

III. CHARACTERIZATION 38

A. Materials 38

1. Film Thickness 38

2. Electronic Structure 39

3. Transmission Electron Microscopy 43

4. Energy Dispersive Spectroscopy 45

B. Devices 46

1. I(V) Characteristics 46

2. Quantum Efficiency 47

3. Urbach Energy 52

4. Tauc Gap 54

C. Modeling 55

D. Device Optimization 61

IV. RESULTS 62

A. Material Quality 62

1. Film Characteristics 62

2. Constant Bandgap Devices 79

B. Device Optimization 94

V. CONCLUSIONS 107

REFERENCES 111

ACNKOWLEDGEMENTS 115

APPENDIX. CONSTANT BANDGAP DEVICE PARAMETERS 116

ABSTRACT

Graded bandgap p-i-n diode solar cells are fabricated with a-(Si,Ge):H deposited by triode PECVD. These cells are optimized for low energy photon absorption, and are suitable for the bottom cell of a tandem cell structure. Initially, a series of a-(Si,Ge):H films with a wide range of germanium contents were grown to determine the alloyed material quality. The techniques used to characterize the material include electrical and optical measurements, as well as EDS, TEM and SEM analysis.

Reproducibly high quality films were deposited using low chamber pressures (~20mTorr), high levels of hydrogen dilution, substrate temperatures around 300 °C, and a negative substrate bias. The variation in material characteristics with germanium content is reported including dark- and photoconductivity, subgap absorption, Tauc gap and activation energy.

A series of constant bandgap devices were also fabricated to determine the hole transport parameters, as well as the Urbach energy. A new computer model for the internal electric fields is used to analyze the device results. The model determines the quantum efficiency from the internal electric field profile and the hole transport parameters.

The hole mobility lifetime product ($\mu\tau$) has not been well characterized in a-(Si,Ge):H, and is quantified for the first time here using the computer model. The

quantum efficiency values are accurately modeled by adjusting three parameters: the interface electric field, the p-layer absorption and the hole $\mu\tau$ product. Once the hole $\mu\tau$ product was determined for various levels of germanium content in the i-layer, an exponential relationship between the Urbach energy and $\mu\tau$ was found. This relationship is most likely due to the dispersive transport of holes in the valence band, and provides researchers with a new tool for determining the $\mu\tau$ product.

The model was also used to guide the design of the optimized graded bandgap devices. A series of devices were then fabricated and tested. The devices with the best results had a multiple graded i-layer with a minimum bandgap energy of about 1.46 eV, and a thickness of about 0.4 μm. The final optimized structure had an approximately 25% improvement in long wavelength quantum efficiency.

I. INTRODUCTION

A. Amorphous Silicon Photovoltaics

The work presented here focuses on the low bandgap cell of a tandem solar cell structure. This cell is made with an amorphous silicon-germanium alloy, which generally does not have the high transport parameters that pure a-Si:H has.[30,35] Also, the material is not as well characterized, since it has not been made with reproducible material parameters on a wide-spread basis.[34] To increase a-(Si,Ge):H solar cell efficiency, this project follows three main directions; improving the material quality in a reproducible way, improving the solar cell device design including bandgap grading, and computer modeling of material parameters and device conditions to optimize the efficiency. Plasma-enhanced chemical vapor deposition (PECVD) is used as the deposition technique, with the reactor configured in a triode geometry. Each of these research directions will be explained in detail as well as the experimental methods and material and device results in the following chapters.

Hydrogenated amorphous silicon (a-Si:H) is a valuable and relatively new semiconductor technology that has attracted worldwide attention in research and industrial applications. This material and its alloys can easily absorb photons in the visible wavelength range and can be deposited in large areas on uneven or flexible surfaces. These properties make a-Si:H a uniquely capable photoreceptor. After its

introduction as a device quality semiconducting material in the late 1960's, a-Si:H quickly appeared in many new products. A-Si:H applications include photovoltaics, thin-film transistor arrays and memory devices, electrophotography, image sensors and most recently field emission devices for flat panel displays.

As a form of clean, renewable energy, a-Si:H photovoltaics is a rapidly expanding market both in the United States and internationally. Photovoltaic systems are particularly well suited to meet the rapidly increasing electrical demands in developing countries. Some of the advantages provided by photovoltaic systems include low installation costs, low maintenance costs and little impact on the environment. In the U.S., state and federal legislation has encouraged the use of renewable energy sources to reduce pollution and to lower dependence on foreign supplies of fossil fuels.

The concept of using amorphous silicon for photovoltaic systems was first proven in 1971 with the fabrication of solar cells that had a three percent conversion efficiency.[1] Today, stable efficiencies have reached 8-9% for large area cells. These cells are suitable for many terrestrial applications ranging from calculators to remote-location power production. Further improvements in solar cell efficiency would expand the role of a-Si:H in the renewable energy market. The potential future uses of a-Si:H photovoltaics include the replacement of expensive electric grid line extensions, electric car recharging stations, and homeowner rooftop installations.

For a photovoltaic material to be economically viable it must be abundant, safe for the environment, and efficient enough to outweigh its production costs. A-Si:H based solar cells are well suited to meet these conditions, but the relatively low efficiencies characteristic of these cells have limited their use to small area applications thus far. The efficiencies reported in the literature for a-Si:H based solar cells are metastable efficiencies. The initial efficiency of a cell may be 10 to 12 percent or higher, but this value degrades over extended exposure to sunlight to the lower, metastable efficiency. Increasing this metastable efficiency is the focus of researchers in both industry and academic institutions, and, through the use of improved deposition techniques and bandgap engineering using alloys, is the focus of this work.

B. Overview of a-Si:H Research

Initial work on a-Si:H proceeded slowly, but as the number of potential applications became known, research greatly expanded. The properties of pure amorphous silicon have been known for many years, but this material is highly defective with large densities of midgap recombination states and is inappropriate for electronic devices. Device quality material is made by the introduction of hydrogen into the amorphous silicon network. Chittick et al. were the first to make hydrogenated amorphous silicon in 1969.[2] They used the glow discharge deposition technique, also known as plasma-enhanced chemical vapor deposition or PECVD, that

has become the industry standard, although the design of their reactor has been greatly improved since that time. They did not follow through on their work and the subject was dropped for several years. Then, Spear and Lecomber recognized the potential of a-Si:H in 1972, and restarted film depositions.[3] By 1975, Spear and Lecomber had achieved both p-type and n-type doping by adding boron and phosphine to the a-Si:H material.[4] This development made device fabrication possible and led to the rapid expansion and wide interest in a-Si:H technology found today.

Carlson and Wronski led the initial work on a-Si:H based solar cells by depositing p-i-n diodes on stainless steel substrates.[1] Initial efficiencies were poor (~3%), but improved steadily with improvements in deposition technology. The degradation of material quality and metastable efficiencies after exposure to sunlight was first documented by Staebler and Wronski in 1977.[5] The understanding of the possible sources of this instability has advanced considerably, but no definite solution to this problem has yet been found.

The rapid technological advancement of a-Si:H over the next sixteen years has exceeded our basic scientific understanding of the material. Many new products successfully incorporate the material, while research into the physics of a-Si:H has been slowed by two problems. First, unlike crystalline silicon, a-Si:H material characteristics are highly dependent on deposition conditions and even on measurement conditions. As a result, characteristics found by one research group may

be entirely different from those of another group. This problem is diminishing since researchers are taking more care to report all deposition parameters and measurement conditions. Unfortunately, it is still generally found that improvements in material quality in research labs do not necessarily translate into improved solar cell devices at the production line level due to differences in the deposition conditions.

The second problem arises from the fact that internal strain causes a-Si:H to flake off its substrate if the deposited layer becomes too thick. As a result, the thickness limit on depositing films is in the 2-3 micron range. Measuring the bulk properties of such thin films is difficult since surface effects may dominate. Much of the older data on a-Si:H is now suspected of being largely influenced by surface properties rather than measuring strictly bulk properties. New techniques for measuring the properties of a-Si:H have become popular and are leading to better understanding of the material. Some of these techniques are described in this work.

Advances in material quality and improved device designs will both be necessary to increase a-Si:H solar cell metastable efficiencies. Currently, both industrial and academic groups are working on a-Si:H research, although very few academic groups are actively working on device fabrication. In the U.S., the National Renewable Energy Laboratory (NREL) has coordinated federal and industrial funding for the Department of Energy by setting research and production goals. NREL has also provided a forum for cooperation among federally funded research groups to enhance

the development of the technology. Some of the research directions are described next.

Various a-Si:H based device structures are used in solar cell modules. Stacked p-i-n solar cells of successively lower bandgap have achieved the highest reported efficiencies.[6] The different layers of a tandem cell structure are made with alloys of a-Si:H, as outlined in detail in section E. A continuous range of bandgaps from ~2.3 eV to ~1.1 eV can be achieved in amorphous semiconductors by incorporating elements such as carbon and germanium during deposition. For devices, though, this range in bandgaps is restricted by the reduction in material quality that occurs with increased alloy concentration.

Alloys also provide a means for grading the bandgap within a single cell. Graded bandgap cells have higher internal electric fields and improved photocarrier collection that increases the metastable efficiency over cells with constant bandgaps.[7] Many combinations of bandgap grading and tandem cell structures are possible with a-Si:H alloys, and computer modeling has become a popular technique for optimizing the design of these structures. Device computer modeling is a useful method for comparing the design of various structures, but is restricted somewhat by our lack of understanding of the basic material properties. The computer model used in this work takes a simplified approach to computing the photocarrier collection of a p-i-n structure and has successfully predicted experimental results. Models that attempt to

include every possible material parameter are not usually as successful and are highly dependent on the particular deposition system in use.

C. Properties of a-Si:H

1. Continuous Random Network

Amorphous silicon is a fundamentally different material from crystalline silicon, although the silicon bonds create a similar semiconducting electronic structure. Complete reviews of the current understanding of amorphous semiconductor material properties are included in the references (8-11), and a brief overview is presented here. Amorphous silicon does not have a crystal lattice, so the traditional means of explaining the electronic band diagram using Bloch waves, Brillouin zones and lattice parameters do not apply. Instead, a more basic approach using the bonds found in the amorphous structure is generally used.

Amorphous silicon is best described as a continuous random network that has short range order, but no long range order.[12] Silicon atoms, having four valence electrons, bond covalently to four neighboring silicon atoms with the same average bond lengths and bond angles as in crystalline material. This four-fold coordination only extends for a short distance, though. Disorder in the form of variations in the bond lengths and angles destroys the symmetry after a few interatomic spacings. These variations in bond dimensions also allow atoms in the network to have a variety

of correlation numbers. This randomness is what makes amorphous silicon uniquely capable as a photovoltaic device, but may also be the source of the inherent instability of the material.

Variations in bond dimensions and correlation number are shown in the schematic network model of Figure 1.1. A silicon atom that has a coordination number of three has one unpaired electron, known as a dangling bond. These dangling bond defects create an electronic energy state that appears near the center of the semiconductor energy gap. It is this type of defect that makes pure amorphous silicon unusable for electronic devices.

When hydrogen is present during the formation of the network, it effectively

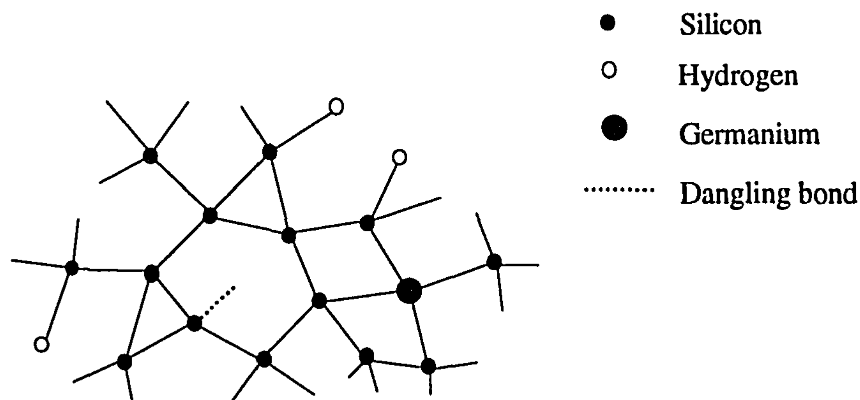

Figure 1.1. Representation of the hydrogenated amorphous silicon continuous random network and the incorporation of germanium

removes the dangling bond defect by bonding with the unpaired silicon valence electron. A hydrogen concentration of approximately ten atomic percent is required to reduce the dangling bond defect density to device-quality levels. A higher concentration of hydrogen reduces the material quality by promoting the formation of weak Si-H bonds and creating microvoids containing high concentrations of hydrogen. Lower concentrations of hydrogen, on the other hand, leave too many dangling bond defects in the material.

Also depicted in Figure 1.1 is the incorporation of a germanium atom. The network easily accommodates atoms of different bond dimensions, allowing the continuous variation in the energy gap that is possible with alloying. Varying the germanium content changes the energy gap linearly between that of pure a-Si:H and pure a-Ge:H. The same is true for the incorporation of carbon into the network. These alloys are used to enhance photon absorption and photogenerated carrier collection through the use of bandgap engineering.

Unfortunately, introducing atoms other than silicon or hydrogen degrades the quality of the material. Both the electrical and structural properties of a-(Si,Ge):H degrade with increasing germanium content, limiting the useful range of bandgaps available for devices.[13] The practical lower limit for the bandgap is about 1.4 eV for solar cell devices. It has been reported that the properties of pure a-Ge:H are better than the alloy properties, although far different deposition conditions are used than

those used for a-Si:H deposition.[19] This is encouraging since it may indicate that the alloyed material can be improved if the proper deposition conditions can be found, rather than the possibility that germanium simply has intrinsically higher defect levels.

Another aspect of the continuous random network of amorphous semiconductors is the lack of indirect or momentum assisted recombination paths. In crystalline semiconductors, indirect recombination paths along a crystal axis sometimes define the energy gap since the energy for this path is lower than the direct recombination path. This is not true in a-Si:H since it has no crystal axes. As a result, a-Si:H is always a direct bandgap material. Depending on hydrogen content, the bandgap energy of a-Si:H is in the 1.7 eV to 1.8 eV range. This value is lower than the 3.0 eV for the direct bandgap of crystalline silicon and results in significantly higher absorption coefficients for photons in the visible wavelength range.

The explanation for why the direct bandgap energy of a-Si:H is lower than the crystalline silicon direct bandgap is again due to the disorder of the amorphous network. The four valence electrons of an unbound silicon atom occupy two 3s and two 3p electronic orbitals or energy states. When the silicon-silicon bonds form during deposition, the electron interaction splits these energy states into bands. The highest energy band occupied by electrons becomes the valence band, and the next higher band becomes the conduction band. When the bond energies vary due to differences in bond length or angle as in the amorphous network, the electron

interactions create a wider range of allowed electronic states, and the energy bands become broader. As a result, the top of the valence band moves up in energy and the bottom of the conduction band moves down in energy as compared to the crystalline energy bands. Then, the resulting bandgap for the amorphous silicon network has a lower energy value than in the crystalline material.

The presence of hydrogen in the network also affects the electronic structure. The incorporation of hydrogen reduces the band broadening by passivating dangling bonds and removing some of the weak silicon bonds, so the a-Si:H bandgap is increased somewhat by increasing the hydrogen content. Varying the hydrogen content only provides about a tenth of an electron-volt of useful change in the bandgap, though, since straying too far from the optimum hydrogen content increases the defect density, as explained earlier. Therefore, hydrogen variations can only be used to produce bandgap grading in the top or middle cell of a tandem cell structure. Alloying is required to achieve the lower bandgaps needed for the bottom cell. One method of easily controlling the hydrogen content is to change the deposition temperature while holding all other parameters constant. This method is a useful way to grade the bandgap in the first two cells without using the lower quality alloys.

2. Metastability

As mentioned in the first section, the a-Si:H solar cell efficiency will degrade when the cell is exposed to sunlight. It has been found that any form of excess carrier injection will reduce the transport properties of the material.[10] It is generally thought that the various alternative bonding configurations allowed in an amorphous network is the source of this instability. The initial bonding configuration may change to a new metastable configuration that is less conducive to electron and hole transport, but such a change would require a source of energy. The excess energy from electron-hole recombination is a likely energy source, but how this energy is transferred and the exact form of the initial and final amorphous network is still a subject of debate. Several models have been proposed but none has gained universal support.[10]

It is known that the defect density initially increases when excess carriers are injected, and then levels off at a new metastable density. The original defect density can then be nearly recovered after thermal annealing. Most models explain this phenomenon in terms of changes in coordination among the silicon-silicon and silicon-hydrogen bonds. Weaker silicon-silicon bonds may be broken by the electron-hole recombination process. The broken bonds form dangling bond defects that provide effective midgap recombination paths for photogenerated carriers. Thermal annealing may increase the hydrogen diffusion in the material allowing silicon-hydrogen bonds to reform at the dangling bond defects and return the defect density to its original value.

3. Electronic Structure and Transport

The energy band diagram of a-Si:H is created by the electron orbital interactions between the various types of bonds in the network. The disorder in the network creates a continuous distribution of allowed energy states that does not have sharp edges near the semiconducting forbidden gap. Designating the energy of the forbidden gap is somewhat ambiguous since there is no 'forbidden' region without allowed energy states. Several different definitions are used to designate a bandgap energy, with some of the more common ones described next.

One method of designating a bandgap is to use the carrier transport properties. The conduction of electrons and holes in the extended states of the conduction and valence bands is impeded by frequent trapping in localized states near the band edges. This method of conduction is known as dispersive transport, and is represented by the diagram in Figure 1.2.[31,33] The localized state density dominates the extended state

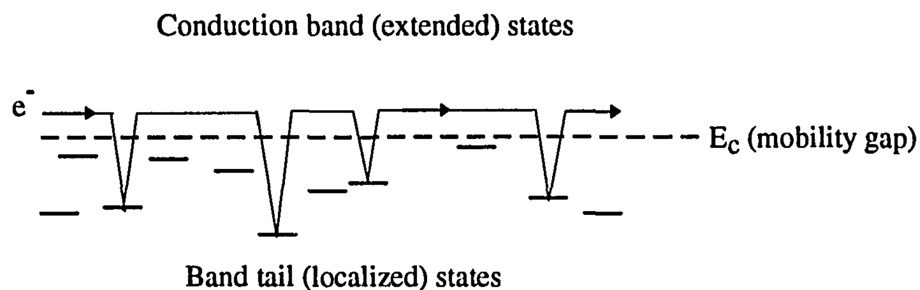

Figure 1.2. Dispersive transport of an electron in the conduction band

density in regions leading up to the conduction and valence band edges. Then, the demarcation between extended states and localized states at each energy band defines a gap known as the mobility gap. Measuring the value of the mobility gap is difficult, though, therefore this definition is not used as often as some of the other methods.

The localized states below the conduction band and above the valence band are known as band tails and have an exponential energy distribution. The density of extended states and band tail states also determine the absorption of photons, which provides another way of defining the bandgap. The absorption coefficient depends on the extended state density distribution, which may be approximated as parabolic near the band edges. Then the absorption coefficient follows the relation

$$\sqrt{\alpha h\nu} = B(h\nu - Eg) \tag{1.1}$$

where α is the absorption coefficient for a photon of energy $h\nu$, B is a material dependent prefactor and E_g is the bandgap.

The above approximation was made by Tauc et al. and is not considered entirely correct, since the bands may not be parabolic at the edges.[10] This bandgap, known as the Tauc gap, does however provide a simple experimental means for comparing the energy gap of various samples, and will be used in this work. One other method of

defining an energy gap is to simply designate the energy where photon absorption reaches a value of 10^4 cm^{-1}, and is known simply as the E_{04} gap.

The electronic structure is completed by including deep level states as shown in Figure 1.3. Both the band tails and deep level states are generally modeled as exponentials. The slope of the valence band tail states is always somewhat lower than the conduction band tail slope. The absorption coefficient for photons with energy less than the Tauc gap follow the relation

$$\alpha = \alpha_0 \exp\left(\frac{h\nu}{E_\mu}\right) \qquad (1.2)$$

where $h\nu$ is the photon energy.

The characteristic energy E_μ is known as the Urbach energy, which closely

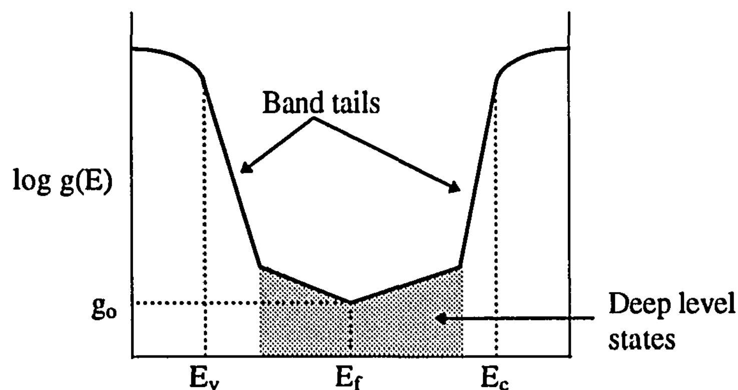

Figure 1.3. Energy distribution of the density of states

approximates the slope of the valence band tail, shown as the first exponential region next to the valence band in Figure 1.3.[10,29] The Urbach energy is one measure of material quality, since a high-quality a-Si:H network will have lower defect densities, which translates into narrower band tail distributions.[26] Values of around 45 meV for E_μ are found for high-quality a-Si:H, with alloys having somewhat higher values due to increased disorder.[22] The Urbach energy is relatively easy to measure, compared to other material quality measurements such as ESR, photothermal deflection spectroscopy, deep level transient spectroscopy and small-angle x-ray spectroscopy. Establishing the correlation between this parameter and other material parameters such as the alloy content, transport parameters and optical characteristics would provide researchers with a useful new technique for estimating alloyed material quality. Finding a correlation will be one of the goals of this project.

The deep level density of states shown in Figure 1.3 is created by defects in the material such as dangling bonds. In hydrogenated material, these deep defects have a low density and the firm level can easily move within this region. The Fermi energy of intrinsic material is located near the minimum in defect density g_o, which is slightly closer to the conduction band than the valence band.[32] The exact distribution and source of these deep level energy states are still the subject of ongoing debate. The exponential distribution shown in Figure 1.3 is a simple way to model this region of the energy diagram and results in good correlation with some of the experimental

results. This deep level defect distribution is used in the computer model described in chapter 3. More sophisticated distributions such as the mid-level gaussian distributions of the defect pool model are often currently used to explain all of the experimental results, but these models do not necessarily provide a better means for designing higher efficiency solar cell devices.[27,28]

D. A-Si:H Growth

Low temperature (<400 °C) a-Si:H growth in a PECVD system occurs by chemical reactions between incident energetic ions and radicals from the plasma discharge and the growing surface. A depiction of the dominant surface reactions is shown in Figure 1.4. As shown in the figure, the growing surface is covered with hydrogen, which must be removed before silicon atoms can join the network. The removal of hydrogen can occur by several reactions (a, c, d), while the insertion of silicon occurs primarily by reaction b.

Other molecules may contribute to a-Si:H growth including SiH and SiH_2, but are not usually present in large amounts, since these molecules require high energy collisions for their formation. The dominant reactions that contribute to the growth of the network will depend on the deposition conditions in the reactor chamber including substrate temperature, chamber pressure, plasma power and the gas flow rates. The substrate location and bias voltage also affect the growth properties.

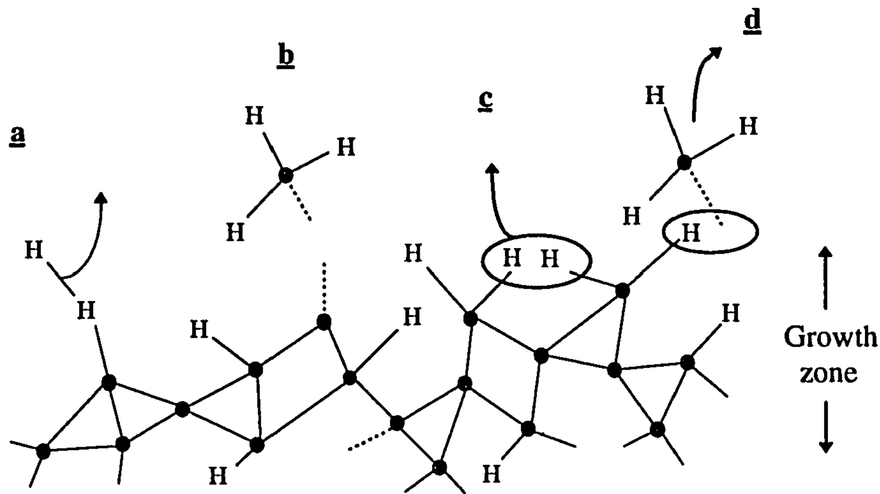

Figure 1.4. A-Si:H surface reactions; a) removal of hydrogen by atomic hydrogen, b) insertion of SiH_3 at an unpaired silicon bond, c) formation and desorption of H_2, and d) removal of hydrogen by SiH_3 forming SiH_4

The silicon-silicon bonds created at the surface become part of the network as they become buried below the growth zone. Weak silicon-silicon bonds present at the surface can be incorporated into the network in this way. Hydrogen can diffuse deeper into the network during growth and passivate silicon dangling bonds that may be left behind. As a result, growing high-quality material is achieved by removing most of the weak silicon bonds at the surface so that they do not contribute to instability later, and also by providing adequate hydrogen to the network during growth. Providing excess energy to the growing surface in the form of ion bombardment (by biasing the substrate) may also improve the alloys.

E. Device Design

High efficiency a-Si:H photovoltaic modules commonly have a three-cell tandem structure as shown in Figure 1.5. The advantage of using a tandem cell structure is that the individual cells can be made thin, which results in a higher internal electric field in the individual i-layers. Then, increased defect levels over time do not have as large of an effect on the efficiency. Also, the bandgap of the individual cells can be varied to match the energy of the predominant photons in that cell, which minimizes thermalization losses and increases absorption. As a result, both the efficiency and stability of a tandem cell device are improved over single junction cells.

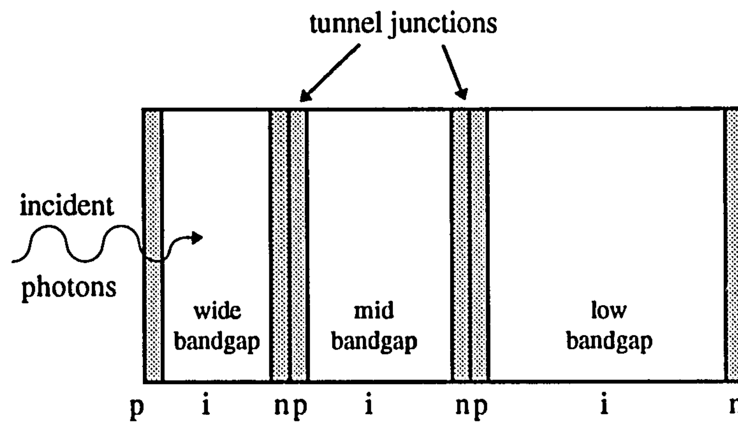

Figure 1.5. Schematic representation of a tandem solar cell device

Graded bandgap structures can be used to further increase the efficiency of the various individual layers of the tandem cell. Figure 1.6 is a comparison of the band diagrams of two low bandgap p-i-n cells biased under operating conditions. This low bandgap cell, in particular, can be improved considerably by grading the i-layer with a combination of a-Si:H and a-(Si,Ge):H.[15] Proper grading schemes will provide an extra electric field in the i-layer for better carrier collection. A graded buffer layer at

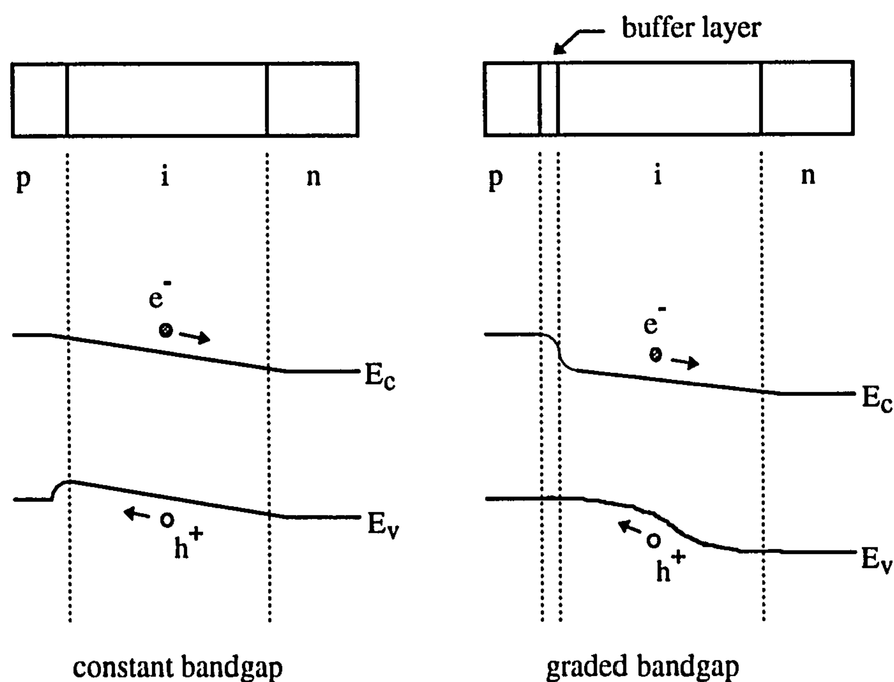

Figure 1.6. The band diagram of a constant bandgap cell and of an improved cell with grading in the i-layer and in an additional p-i interface buffer layer

the p-i interface will also improve the efficiency by eliminating any hole traps in the valence band that increase electron-hole recombination. The depiction of a hole trap is shown at the p-i interface of the constant bandgap cell in Figure 1.6

Various bandgap grading schemes have been proposed, beginning with the simple profile (a) shown in Figure 1.7.[17] With a better understanding of the internal electric field profile in the i-layer, new grading schemes have been introduced (b, c).[18,7] The optimum graded profile will depend on the intended application of the cell and on the material quality at the production line. Computer programs are often used to aid in the design of solar cells since the internal electric fields are highly non-uniform and require numerical analysis to simulate. Also, graded bandgap devices will have non-uniform

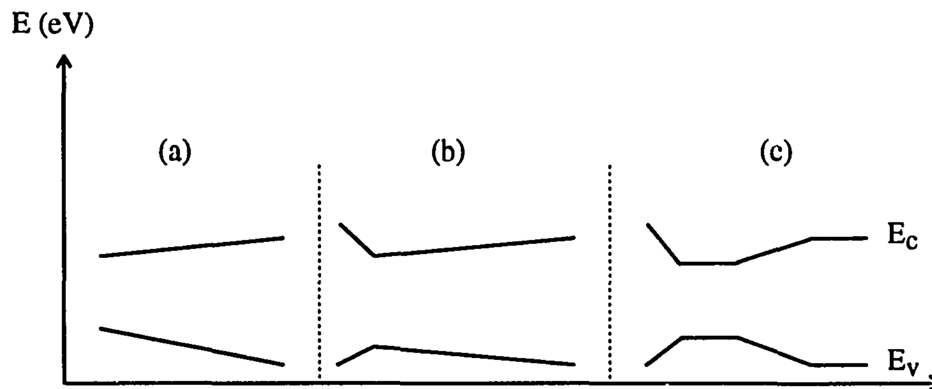

Figure 1.7. Graded bandgap i-layer profiles that improve the efficiency of p-i-n solar cell devices

material parameters since the alloy content changes throughout the i-layer. The computer program used for this work can accommodate spatial variations in the material parameters throughout the i-layer, and is used to evaluate various i-layer bandgap profiles.

F. Scope of Research

This work focuses on the low bandgap cell of a tandem cell structure. This cell is made with an amorphous silicon-germanium alloy, which generally does not have the high transport parameters that pure a-Si:H has. Also, the material is not as well characterized, since it has not been made with reproducible material parameters on a wide-spread basis. To increase a-(Si,Ge):H solar cell efficiency, this work follows three main directions; improving the material quality in a reproducible way, improving the solar cell device design including bandgap grading, and computer modeling of material parameters and device conditions to optimize the efficiency. Plasma-enhanced chemical vapor deposition (PECVD) is used as the deposition technique, with the reactor configured in a triode geometry. Deposition conditions such as substrate temperature and bias, gas flow ratios and chamber pressure are studied to produce the highest quality material.

Material quality is determined from films of pure a-Si:H and a-(Si,Ge):H alloys deposited on glass and conducting SnO_2 substrates. Constant bandgap devices are

also fabricated and used to study device conditions on material quality, and to investigate the hole transport properties. Optical and electrical measurements are also made to determine transport properties and the electronic band structure. Energy dispersive spectroscopy is used to determine alloy composition. Finally, the effects of alloying on the microstructure are studied in the a-(Si,Ge):H films using transmission electron microscopy.

Computer modeling is used to both help characterize the material and to guide the design of new device structures. The model was introduced in this author's master's thesis, where it is described in detail. Also, the FORTRAN program is included in the appendix of the thesis.[15] Devices with various bandgap grading schemes are then fabricated to determine the best i-layer structure. New material and device characteristics are also determined by the model including the hole mobility-lifetime product and the interface electric fields in a p-i-n device structure. Estimates for the midgap defect density distribution and p-layer parameters are also obtained with the model, and are summarized in chapter 4.

Chapter 2 outlines the film and device preparation conditions used to investigate the material parameters and to produce the alloyed material used for the devices. The PECVD deposition system is described in detail, as well as further details about the plasma conditions and characterization. Chapter 3 describes all of the material and device characterization techniques used in the course of this work. The computer

model is also described briefly. The results of the material characterization are presented in chapter 4. These results are used to design the optimum a-(Si,Ge):H graded bandgap structure, which is also described in chapter 4. Finally, the conclusions drawn from this work are given in chapter 5, along with suggestions for future work in this area.

II. SAMPLE PREPARATION

A. Deposition System

All of the films and devices fabricated for this work were made in a capacitively-coupled rf glow discharge reactor. A schematic diagram of the reactor chamber is shown in Figure 2.1. This type of reactor has been used for plasma-enhanced chemical vapor deposition (PECVD) for many years and is well characterized. Most commercial production of a-Si:H makes use of this type of deposition system. Other types of deposition techniques such as electron-cyclotron-resonance and hot-wire reactors are still primarily used only at the research level.

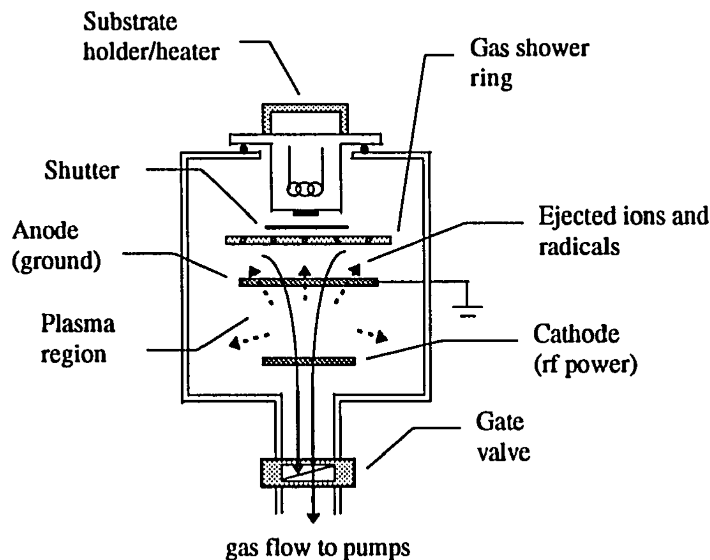

Figure 2.1. Schematic diagram of the PECVD deposition chamber

The plasma is created by the transfer of electrical energy at the electrodes to electrons in the vacuum chamber gases. The electrons gain most of the energy supplied by the rf generator since they are more mobile than the heavier molecules. Energy is transferred from the electrons to the larger gas molecules in the chamber by inelastic collisions. One of the most common reactions created by these collisions is the excitation of bound electrons, which subsequently create the plasma glow when they return to the ground state of the gas molecules. Another reaction is the formation of smaller molecules when the bonds in the precursor molecules are broken by collisions. A wide variety of molecular species can be created in the plasma region including chemically reactive ions and radicals.

A space charge region of net positive potential known as the plasma sheath develops at the edges of the plasma due to the rapid loss of electrons from the plasma to the grounded walls and anode grid. This plasma sheath will eject any positive ions and radicals that diffuse into it from the plasma, creating the discharge that results in film growth. These ejected molecules react with any surface they come in contact with, or they may collide with molecules in their trajectory and form new molecular species.

A wide range of chamber pressures, gas flow rates, plasma excitation powers and frequencies are possible in PECVD, as well as various electrode geometries. The excitation frequency for the reactor used for this work is 13.56 MHz, as are most

reactors in the U.S. due to Federal Communications Commission's regulations. The bottom electrode (cathode) is the powered electrode, while the upper anodic electrode is grounded to the chamber walls. The plasma is contained between these two electrodes and deposition occurs at any surface within line-of-sight of the plasma.

The substrate is located above the upper electrode on a resistively heated stainless steel block. This triode geometry allows the material growth to occur away from the damaging high-energy electrons in the plasma. Also, the substrate is located out of the gas stream since it is above the gas source and the pumps. This limits the chance that any powders (long chains of silicon atoms) that may be formed in the chamber will impinge upon the growing surface and become incorporated into the material.

The substrate holder is insulated from the rest of the chamber and can be biased to induce low-energy ion bombardment. This method of providing extra energy to the growing surface is used to improve the quality of the silicon-germanium alloys, as will be seen in chapter 4. The substrate is heated by a resistance heater attached to the substrate holder. A mask holds the substrate tightly against the substrate holder with four stainless steel, vented cap screws.

Temperature is regulated manually during deposition by monitoring a thermocouple embedded in the substrate holder. Although this method does not measure the temperature of the growing surface directly, it provides an effective means of reproducing the deposition temperature from one run to the next. It is

expected that the temperature of the growing surface will be somewhat lower than the temperature at the thermocouple. This temperature difference is on the order of ~50 °C or less for the temperature range used in this work.

The system is pumped by a turbomolecular and mechanical pump system. Base pressures in the reactor chamber are measured by a tungsten filament ion tube, and are typically in the mid 10^{-7} torr range. The pressure during deposition is controlled by the gas flow rates and by a manual gate valve between the turbo pump and the chamber. This pressure is typically 15 to 30 mTorr and is monitored by an MKS Baratron gauge. The precursor gases are plumbed into the shower ring inside the reactor chamber through a large (0.5 inch) diameter gas tube and mixing manifold.

The manifold is located near the reactor chamber to reduce the possibility of contaminates such as boron from a p-layer deposition from diffusing out of the manifold during the critical i-layer deposition. The manifold is also routinely purged with argon, silane and hydrogen after the deposition of a doped layer and during the initial pump-down. These methods of reducing cross-contamination are very important for a single-chamber system since low defect densities and low impurity levels in the i-layer are critical for high efficiency p-i-n solar cells.

A log of all processing steps, gas purges and plasma parameters is kept with the system. The total run time is recorded after every deposition to determine when the next reactor cleaning is due. The upper electrode is replaced after every fifty hours of

run time. The lower electrode does not become as heavily coated during processing since it is subjected to high-energy ion bombardment due to its large negative bias, and does not require cleaning as frequently. The entire system is cleaned after 150 hours of operation. These periodic cleaning steps are important to maintain consistent plasma conditions and a-Si:H growth rates. The growth rate can drop rapidly when the upper electrode and chamber walls become heavily coated with silicon and will cause the various layers in a device to become too thin. The cleaning schedule implemented for this reactor results in only small changes in the growth rate of ten percent or less between the first run and the last.

B. PECVD Processing

One hundred percent (undiluted) silane gas (SiH_4) is used as the process gas for all of the a-Si:H films and devices. For most of the processing, SiH_4 is diluted inside the deposition chamber with hydrogen. To create the n-type amorphous material for the device fabrication work, phosphorous is added to the plasma chamber in the form of PH_3. P-type material for the initial window layer is made by introducing either diborane (B_2H_6) or trimethylboron ($B(CH_4)_3$) to the plasma. Methane (CH_4) and 10% germane (GeH_4) in hydrogen are used to create the alloys for bandgap grading and enhanced photon absorption. A schematic diagram of the device structure deposited on a tin-oxide coated glass substrate is shown in Figure 2.2.

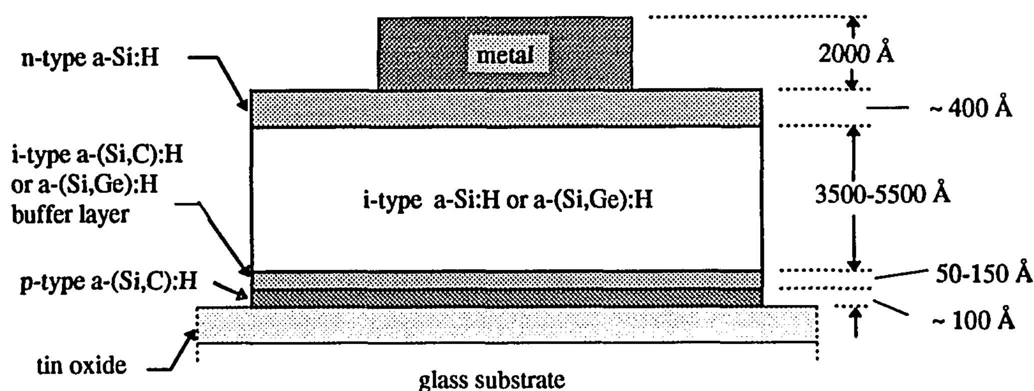

Figure 2.2. The superstrate p-i-n diode device diagram

The initial p-type layer is fabricated with wide-bandgap a-(Si,C):H to allow most of the incident photons to pass through into the i-layer. Any photons that are absorbed in the p-layer do not generate photocurrent since the minority carriers immediately recombine. A buffer layer is then deposited to limit the diffusion of boron from the p-layer into the i-layer during subsequent deposition. Also, the buffer layer improves the device characteristics by providing a smooth transition from the wide bandgap p-layer to the narrow bandgap i-layer. A more detailed explanation of the device structure will follow in chapter 3.

The concentration of each atomic species incorporated into the material depends on the gas flow ratios of the precursor gases into the chamber, which is monitored by

mass flow controllers. All of the depositions are done at low temperature (<400 °C) to prevent thermally activated deposition. The substrate is heated to increase the mobility of hydrogen at the surface, which increases the pacification of dangling bond defects. Also, the thermal energy supplied to the growing surface helps to reduce the number of weak silicon bonds incorporated into the amorphous network by breaking these bonds before they become buried. The effects of temperature on the growth of amorphous silicon-germanium, though, has not been well characterized in the literature.

The plasma is characterized by the rf power supplied by the generator, the dc cathode potential and the peak-to-peak voltage of the incident rf waveform. The power supplied to the plasma is maximized by reducing the reflected power from the chamber. A matching network between the generator and chamber automatically tunes the reflected power to a minimum. The dc cathode potential is measured by a digital voltmeter connected to the cathode through an rf choke. The cathode potential is created by the collection of the highly mobile plasma electrons on the cathode surface. This occurs solely due to the asymmetry in the sizes of the two electrodes, since there is no external dc bias.

The smaller cathode initially collects a large number of electrons from the chamber gases during the first positive half-cycle of excitation. During the negative portion of the cycle, the cathode collects positively charged ions, but at a much slower

rate since the more massive ions do not gain as much velocity. The anode is able to collect a larger number of positive charges during its negative half cycle since it has a larger surface area. The net result is a build-up of negative charge on the cathode that can be measured as a dc potential as shown in Figure 2.3.

The cathode waveform cycles about this negative dc bias with only a short period of positive voltage, when electrons are collected to balance the number of ions collected during the rest of the cycle. The value of this negative dc bias depends on the incident power supplied to the plasma, and is used to reproduce consistent plasma conditions from one run to the next.

A series of films for material characterization was deposited on cleaned 7059

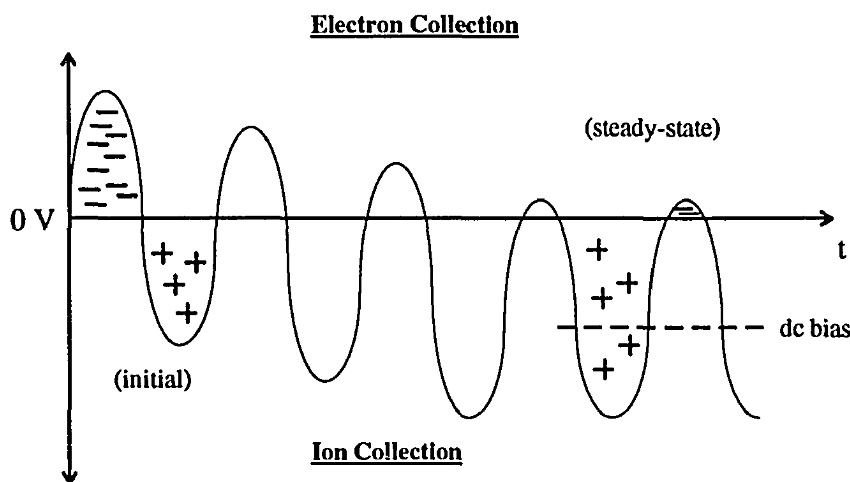

Figure 2.3. Representation of the build-up of negative dc potential on the cathode over the first several rf cycles

Corning glass substrates. The cleaning process for the glass substrates consisted of boiling for ten minutes in detergent and then in an acetone and methanol solution. Several films were also deposited on tin-oxide (SnO_2) substrates to simulate device deposition conditions more closely. The SnO_2 substrates required ultrasonic cleaning in detergent and deionized in addition to the cleaning steps used for the glass substrates. The extra steps were necessary to fully clean the SnO_2 surface prior to deposition.

Once the substrates were loaded into the reactor chamber, a system cleaning process is completed. The chamber is first pumped out with the mechanical and turbo pumps. Then a series of gas purges with nitrogen, argon and silane are done to help remove any remaining moisture from the system. The substrate is heated to a temperature that is at least 50 °C higher than the intended deposition temperature to induce outgassing of impurities from the substrate and holder.

For glass substrates, a cleaning plasma can be lit immediately using silane and hydrogen. This cleaning plasma will etch impurities from the chamber walls and deposit a fresh layer of a-Si:H on all surfaces. A shutter is placed between the plasma and substrate to prevent deposition on the substrate. Tin-oxide substrates must be cooled to 200 °C or less before a cleaning plasma is lit. Although a-Si:H deposition occurs by line-of-sight, energetic hydrogen can diffuse around the shutter and impinge on the substrate surface. The tin-oxide will react with these energetic hydrogen

species if the substrate temperature is too high, or if the plasma is lit for too long, and will no longer make a good ohmic contact. Therefore, the temperature is reduced before the plasma is lit and the cleaning process is limited to fifteen minutes or less.

After the plasma cleaning is completed, the film or device deposition can begin. Device depositions start with a two to three minute p-layer, then a second set of gas purges and a thirty minute plasma clean. The purges are done to help remove any remaining dopant gas from the gas manifold and gas lines leading into the chamber, and the plasma clean covers the walls with intrinsic material, burying any dopant impurities. Once the possibility of cross contamination has been minimized, the i-layer and n-layer depositions are completed. The substrate is cooled to 120 °C or less before removal and metallization.

Table 2.1 lists the typical film deposition parameters used in this work. Several of the deposition parameters were varied over a range of substrate temperatures. The V_{dc} value is the cathode potential, and V_{sub} is the substrate bias voltage. Most of the films were deposited on glass substrates, except for six films deposited on SnO_2 substrates for EDS analysis. Also, a series of films were deposited on specialized carbon-coated copper grid substrates for TEM analysis.

Over fifty devices were fabricated in the course of this research. Constant bandgap devices were made to characterize the transport properties of the silicon-germanium material. Various graded bandgap devices were then made with some of

the typical deposition parameters shown in Table 2.2. A complete list of all of the deposition parameters for the films deposited throughout this project is included in chapter 4. The constant bandgap device deposition parameters are listed in the appendix and the optimized device parameters are included in chapter 4.

Table 2.1. The range of a-(Si,Ge):H film deposition conditions

						Gas	Flow	Rates
V_{DC} (volts)	Pressure (mTorr)	Temp (°C)	Time (min.)	Power (watts)	Vsub (volts)	100% SiH_4 (sccm)	10% GeH_4 (sccm)	100% H_2 (sccm)
-200 to -275	15 to 25	250 to 350	10 to 310	18 to 25	0 , -40	2 to 8	0 to 16	0 to 40

Table 2.2. The range of p-i-n device deposition conditions

						i-layer Gas Flow Rates		
Temp (°C)	p-layer time (min.)	i-layer time (min)	n-layer time (min.)	Power (watts)	Vsub (volts)	100% SiH_4 (sccm)	10% GeH_4 (sccm)	100% H_2 (sccm)
200 to 350	1.5 to 3.0	30 to 75	10 to 15	16 to 25	0 , -40	2 to 8	0 to 16	30 to 50

C. Metallization

To measure the electrical properties of the films and devices, metal contacts are evaporated onto the samples by a thermal evaporator. The evaporator system is a diffusion pumped bell jar with resistively heated metal boats. The bell jar is pumped to a base pressure of less than 3×10^{-6} torr range before evaporation begins.

All of the contacts for the films are made with aluminum deposited through a mask that produces the desired L/W ratio (described in chapter 3) for the conductivity measurements. The aluminum layer is approximately 2000 Å thick as measured by a thickness monitor inside the evaporator. After deposition, the samples are annealed at 170 °C for 15 minutes to improve the contact. Finally, silver paint is applied to provide a good contact to the metal probes.

Metal contacts for the devices are also made in the thermal evaporator. A mask that creates the pattern for both the front and back contact is shown in Figure 2.4. Each circular hole forms a back (n^+) contact and defines the effective area of the solar cell. Contact is made to the p-layer by conduction through the tin oxide substrate and the long metal lines created by the oblong holes in the mask. Resistance losses are reduced by scratching through the a-Si:H to the tin-oxide substrate for each oblong contact before metallization. The device contacts are also annealed at 170 °C for 15 minutes or at 120 °C overnight.

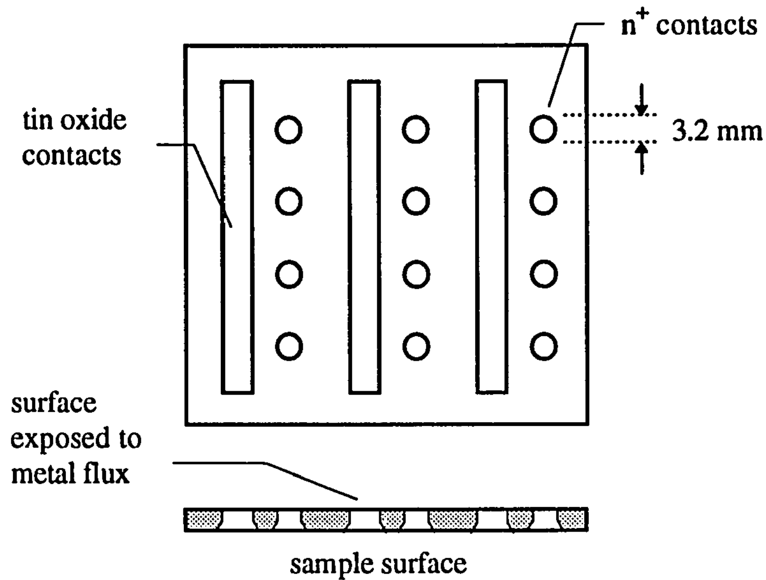

Figure 2.4. Schematic diagram of the solar cell device metallization mask

Aluminum is used for most of the device contacts since it creates a stable ohmic contact. Copper is also used sometimes since it provides improved reflection of long wavelength photons, but this type of contact is very unstable over time and not practical for most analyses. Copper can be used to estimate the current that could be achieved in the devices if they were part of an optimized system with highly reflecting back contacts such as silver-zinc oxide, which were unavailable for this project.

III. CHARACTERIZATION

A. Materials

1. Film Thickness

The thickness of the films deposited on glass substrates was measured in two ways. First, all of the film thicknesses were measured optically using a Perkin-Elmer dual beam spectrophotometer. The interference peaks measured over the wavelength range of 800 nm to 2500 nm follow the relationship

$$t = \frac{\lambda_1 \lambda_2}{xn(\lambda_1 - \lambda_2)} \qquad (3.1)$$

where x=2 for peak-to-peak or valley-to-valley intervals of λ and x=4 for peak-to-valley intervals.[23] The index of refraction (n) will vary with alloy content, and is assumed to be constant over the range of wavelengths used. The value for the index of refraction can be found by fitting several sets of peaks using equation 3.1. The value of n does vary slightly with wavelength, so this method of measuring the thickness is only accurate to about ±0.1 μm.

Second, a Sloan Dektak Stylus profilometer, also with an accuracy of ±0.1 μm was used to confirm the optical thickness measurements on several of the samples. Good agreement between the two methods was obtained. The profilometer also provided an estimate of the thickness of films deposited on SnO_2 substrates. This was

done since the optical technique outlined above does not include the effects of the a-Si:H / SnO_2 interface. The tin-oxide substrates used for this project are not textured, so the profilometer does provide a good estimate of the height of the step at the edge of the films.

2. Electronic Structure

To characterize the electronic structure of the films and devices, a series of measurements are made beginning with the material conductivity

$$\sigma = qn\mu_n + qp\mu_p \tag{3.2}$$

The conductivity of a-Si:H provides information about the electronic structure of the material in several ways. First, since there is a continuous distribution of midgap states in a-Si:H, the Fermi level will always be located somewhere near the center of the bandgap in intrinsic material. An estimate of the position of the Fermi level can be made from the temperature dependence of the conductivity. The formula for $\sigma(T)$ can be derived from the Fermi statistics for electron and hole densities

$$\sigma_{e,h} = \sigma_o \exp\left[-\left(E_{c,v} - E_f\right) / kT\right] \tag{3.3}$$

where $E_{c,v}$ is the conduction or valence band edge defined by the mobility gap, and σ_o is the conductivity prefactor known as the minimum metallic conductivity. Conductivity measurements in intrinsic a-Si:H films are usually dominated by the

electron transport term in equation 3.1 since the electron mobility is an order of magnitude higher and the films are normally slightly n-type.[8]

The Fermi energy E_f can be extracted from an Arrhenius plot of the log of the conductivity over a fairly small temperature range (80 °C to 200 °C). The temperature is kept below 200 °C to limit changes in the band structure. Also, the conductivity is measured in a light-proof box to prevent the photogeneration of charge carriers. The Fermi energy for a high-quality intrinsic sample is nearly equal to half of the mobility gap energy, ~0.8 eV, while lower values for the Fermi energy indicate that increased levels of impurities were incorporated into the material.

Another conductivity measurement that is used to measure film quality is the photosensitivity, which is the ratio of the room temperature photo- and dark conductivity. To determine the photosensitivity, the film is placed in a light-proof box for several hours to ensure that all of the photogenerated carriers have recombined. Then, the dark conductivity is measured by placing a 100 V bias across the metal contacts and recording the induced current. The photoconductivity is measured in the same way except with the sample illuminated by a one-sun intensity light source.

The photo- and dark conductivity is determined using

$$\sigma_{d,ph} = \left(\frac{w}{L}\right)\frac{I}{V \cdot d} \qquad (3.4)$$

where L/W is the length-to-width ratio of the metal contacts and d is the film thickness. The light source used to simulate the sun is an ELH lamp biased at 110 V. This illumination splits the quasi-Fermi levels by exciting electrons and holes to the mobility band edges where they drift to the contacts. The value found for the photoconductivity depends on the intensity of the light, the number of charge carriers lost to geminate and Shockley-Read-Hall recombination, and the dispersive transport of the electrons.[10] Since the light intensity is the same for all samples, the photosensitivity is an indication of how well the material can collect the photogenerated carriers.

Another measurement of the electronic structure of the films is the Tauc gap. An estimate of the Tauc gap can be made using the absorption data from the spectrophotometer. From equation 1.1 in chapter 1, the Tauc gap can be found by plotting the square root of the absorption coefficient times the photon energy on the ordinate and the photon energy on the abscissa. Then, the intercept of the abscissa is the Tauc gap energy. An example of this measurement technique is shown in Figure 3.1, along with a fit to the linear portion of the data. The low energy region of the curve is not included in the linear fit since this data has a large noise component.

The slope of the linear fit from the Tauc plot provides an estimate of the absorption prefactor B of equation 1.1. The prefactor is given by

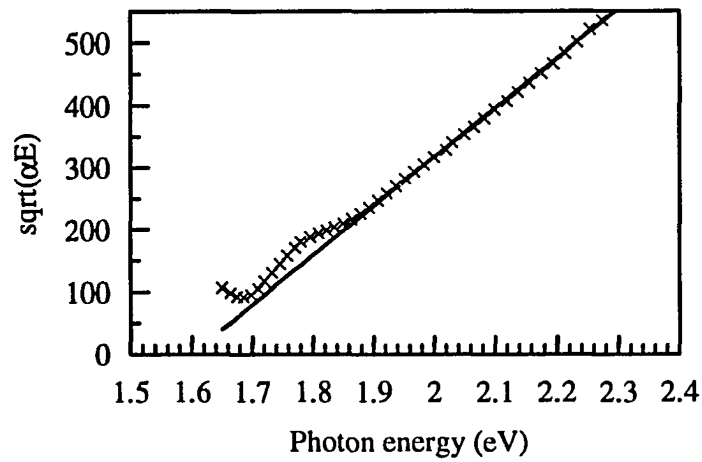

Figure 3.1. Typical Tauc plot of an a-Si:H film, where the solid curve is a linear fit to the data

$$B = \sqrt{\frac{4\pi\sigma_0}{ncE_w}} \tag{3.5}$$

where E_w is the extent of the band tailing.[8] As the material becomes more disordered, the value of E_w increases, and the absorption prefactor B decreases in magnitude. This result is important for modeling purposes since most previous models described in the literature assume a constant value for B. Clearly, B will change depending on deposition conditions and dopant or alloy content, and this change can be found from the Tauc plot data. All of the modeling done for this work includes the dependence of B on germanium content and on deposition conditions as found from the experimental results.

3. Transmission Electron Microscopy

To determine material homogeneity, a series of a-(Si,Ge):H films were prepared for transmission electron microscopy (TEM), and for secondary emission spectroscopy (SEM). The SEM micrographs were featureless for all films, indicating that the substrates were evenly covered during deposition. It was possible to grow these samples with the same parameters as the films prepared for electrical and optical characterization, since SEM is a surface analysis technique and there is no restriction on film thickness. TEM analysis on the other hand, requires thin ($d \leq 200$ nm) samples with no substrate to allow the electron beam to pass through the sample. This limitation on film thickness required a new film preparation method.

Initially, the films were deposited on the same glass substrates as all of the other films. To create a region of material with no supporting substrate, the samples were sliced and layered for subsequent milling. The samples were sliced with a diamond saw to produce approximately 3 mm wide strips of deposited material. During the sawing process, the films would always flake off the substrate and the sample would be destroyed.

The alternative method found for producing the required thickness was to deposit a thin layer of material (~50 nm) on a new type of substrate that could be loaded directly into the microscope. The substrates were 3 mm copper grids coated with approximately 10 nm of carbon. A new substrate holder was made to hold the copper

grids in the deposition chamber, where the thin layer of a-(Si,Ge):H material was deposited with the same parameters as the previous films. It is expected that the growth on these carbon coated substrates will not exactly simulate the film growth on the large glass or tin-oxide substrates due to the small sample size and proximity of the mask. However, this method is very useful for comparing the microstructure of a series of alloy compositions all deposited on these same substrates.

Previous TEM results reported in the literature have indicated that silicon-germanium alloys are not completely homogenous.[13] Regions of approximately 50-100 Å absorb or deflect a larger number of electrons from the electron beam and appear as dark regions in the micrographs. It is not yet known if this heterogeneity is due to germanium-rich regions within the material, or if some other microstructure formation is induced by the presence of the germanium atoms.

Since the preparation conditions clearly play a role in the microstructure formation, a series of films with a range of germanium contents and deposition conditions was prepared. The TEM microscope used for this analysis is a JEOL 100cx. The resolution of this microscope is fairly low, but is adequate for looking at the structure in these bulk films.

4. Energy Dispersive Spectroscopy

Energy dispersive spectroscopy (EDS) is used to estimate the atomic concentration of germanium in another series of a-(Si,Ge):H films. The apparatus used for this measurement is a JEOL JSM 840A electron microscope with a Kevex energy dispersive x-ray detector. The set of samples for this analysis includes a series of films that were deposited with various germanium flow rates, while all of the other deposition parameters were held constant. Another series of films with constant germanium flow rates and with various substrate temperatures was also prepared. All of the films were deposited on conducting tin-oxide substrates, except for one film deposited on glass to isolate any effects that the substrate may have on the film composition.

The films with constant germanium flow rates were deposited at 250°, 300° and 350 °C. The purpose of these films was to determine if the thermal energy at the substrate induced excess germanium growth. It is known that the germanium-hydrogen bond is a lower energy bond than the silicon-hydrogen bond.[14] Thermally activated CVD of germanium produces lower quality films and this process should be avoided for device-quality deposition. Thermal CVD was observed by bandgap analysis in devices deposited at temperatures above 350 °C, so the analysis of the germanium content in this series of films can be used to determine if a similar effect is occurring at lower temperatures.

B. Devices

1. I(V) Characteristics

The I(V) curve produced by a p-i-n diode under illumination determines how well the device will work as a solar cell. A typical plot of the power-producing quadrant of an I(V) curve is shown in Figure 3.2. The point of maximum power production determines the efficiency of the device.

The maximum power point P_{max} divided by the total illumination energy defines the efficiency of the device. The energy of a light source of one-sun intensity is about 100 mW/cm^2, and the area of the cells used in this project are 0.08 cm^2. The light

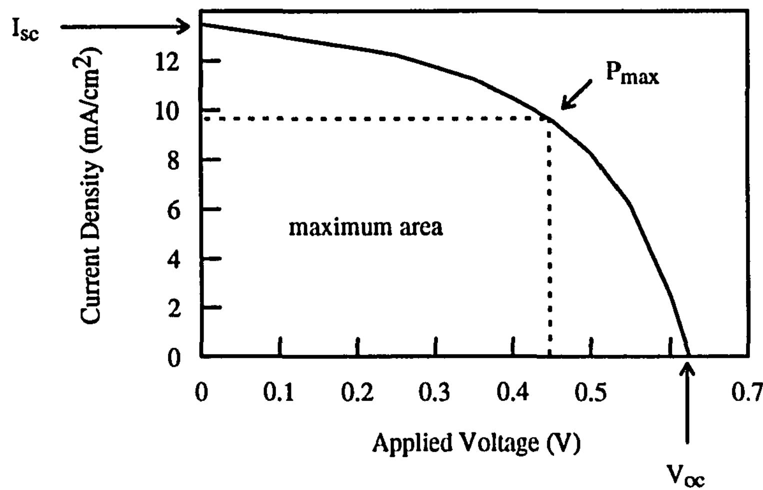

Figure 3.2. Current-voltage relationship of an illuminated p-i-n diode

source used for the I(V) measurement is an ELH lamp biased at 110 V. The open circuit voltage V_{oc} and short circuit current I_{sc} should be maximized to achieve the highest efficiency, and are two more parameters used to compare the devices prepared under various deposition conditions.

Another figure of merit for solar cell I(V) curves is the fill factor, which can be found by dividing the maximum power by the $V_{oc}I_{sc}$ product. The fill factor provides an indication of the quality of the material used in the i-layer, and how well the solar cell is designed. High quality a-Si:H cells with proper p-i interface designs have fill factor values of about 70% or more.[21] This value is less than the percentages that can be achieved in crystalline solar cells since the conductivity of the i-layer is considerably lower in a-Si:H. The fill factor of silicon-germanium cells is generally lower (50-60%). It is not expected that the fill factor of pure a-Si:H cells can be greatly improved, but improvements in a-(Si,Ge):H solar cell fill factors are needed before this system can be used successfully in device fabrication.

2. Quantum Efficiency

The quantum efficiency (QE) measurement is another useful diagnostic measurement of solar cell devices. The QE is defined as the number of charge carriers collected at a particular wavelength divided by the number of photons incident on the sample at that wavelength. QE measurements provide information on how well the

device absorbs photons of various wavelengths, and how well the photogenerated carriers are collected under normal forward-bias operating conditions. The internal electric field is reduced with biasing in the forward direction, and the QE results provide details about how this reduction affects the collection of photogenerated carriers. Also, any problems in the device design that may inhibit carrier collection such as hole traps at the p-i interface can be uncovered with the QE measurements. Finally, the dependence of the QE at a particular wavelength on the bias voltage can be used, in conjunction with computer modeling to estimate the material transport parameters. This technique will be discussed in greater detail in the modeling section.

The QE apparatus is diagrammed in Figure 3.3. For this setup, the monochrometer shown in the figure is used to change the wavelength of the incident photons. The chopper placed between the light source and sample modulates the photon signal to produce a 13 Hz square wave. The lock-in amplifier is tuned to this frequency, which is far from any noise sources that may be present in the setup. The photogenerated current from the devices under test for each incident photon wavelength is amplified and displayed on the lock-in amplifier. A dc light source illuminates the sample to produce the charge carrier densities that are present under normal operating conditions. This dc light source does not contribute directly to the QE since the lock-in amplifier is tuned to the 13 Hz signal.

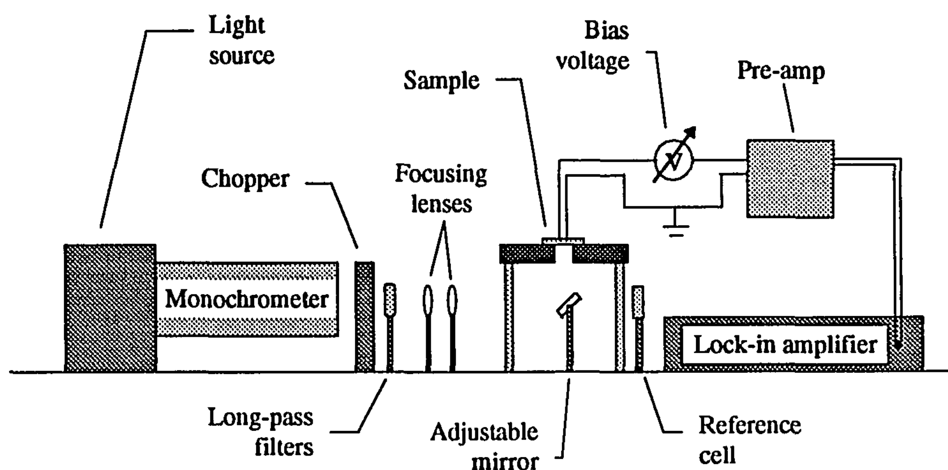

Figure 3.3. Schematic diagram of the quantum efficiency apparatus

The sample can be biased at forward or reverse voltages or be grounded. Typically, the device currents are measured over the visible wavelength range of 400 nm < λ < 800 nm, at steps of 20 nm, since this range covers the major portion of the solar spectrum. The forward and reverse bias voltages can be applied to the cell to simulate operation conditions and to enhance the internal electric field respectively. Longer wavelengths (800 nm < λ < 1000 nm) are used to determine the Urbach energy and Tauc gap using the techniques outlined in the next sections.

The photocurrent produced by the reference cell at each wavelength is also measured to determine the relative light intensity at the various wavelengths. This

intensity can change from day to day, depending on the exact position of the lenses and the condition of the lamp. Since the reference cell is not subjected to the same number of photons as the sample under test, the QE(λ) values are relative. A reference is chosen by arbitrarily setting the peak QE(λ) value. Then, all of the other QE(λ) values are scaled to this reference. Care must be taken when interpreting the QE curves from one sample to the next, since they all have the same peak reference point. This method does provide the correct relationship between the QE(λ) ratios of a particular sample, and from sample to sample.

The ratio of the QE(λ) values to the peak QE value at zero bias voltage provides information about how well the device absorbs and collects the photons of various wavelengths. A large ratio for short wavelength photons ($400 \text{ nm} < \lambda < 500 \text{ nm}$) indicates that these photons are being absorbed in the p-layer and do not contribute to the photocurrent. The p-layer may either be too thick or have a low bandgap. The primary focus of this work will not be placed on any p-layer problems since the cells are intended primarily for the bottom cell of a tandem cell structure. In such a structure, the high energy photons are absorbed in the top layers and do not reach the bottom cell.

The QE ratio for the longer wavelength photons is of particular interest for this project. These low energy photons have lower absorption coefficients (see equation 1.2) and penetrate deeper into the cell. The QE data at lower energies determines how

well the cell can absorb these photons. The QE(λ)/QE(peak) ratio is used to compare the various bandgap devices and grading structures to help determine the best configuration. Also the quality of the entire i-layer material plays a role in the collection of the carriers generated by low-energy photons. To understand how the QE ratios can be used to judge material quality; photon absorption and carrier collection must be looked at in detail.

Since the photons are incident on the p-layer, the lower energy photons are absorbed farther from the p-layer than the higher energy photons. As a result, these photogenerated holes must drift farther across the i-layer before they are collected in the p-layer. As a result, more of these holes will recombine before reaching the p-layer. If the QE ratio at these long wavelengths is low, it is an indication that the recombination is high, or that the photons were not absorbed. If the QE ratio is high, then the device works well for these long wavelength photons.

Since low QE(λ) ratios at long wavelengths could be due to either poor material quality or lack of photon absorption, another technique is used to differentiate between the two. Biasing the cell to a relatively large negative voltage (-0.5 V) will increase the internal electric fields so that holes generated near the back of the i-layer are more likely to be collected, regardless of material quality. Then, the ratio of the negatively biased QE values to the zero volt QE at a particular wavelength can be used to determine i-layer quality. Large QE(V) ratios indicate that the holes were generated

but were not being collected without the extra field-assist provided by the negative bias. Low QE(V) ratios indicate that the material is of high enough quality to collect the holes even at zero bias voltage.

Then, if the long wavelength QE(λ) ratio is low, indicating a problem, but the QE(V) ratio is low, indicating good material quality, the problem can be pinned on low photon absorption. Since the cells are designed to be the bottom cell of the tandem cell structure, good long-wavelength photon absorption is required. The absorption of these photons can be increased by lowering the bandgap in the i-layer and by increasing the i-layer thickness. Both of these techniques reduce the internal electric fields, though, and consequently reduce hole collection. Designing the optimum bandgap structure then becomes a matter of finding the best trade-off between these two limitations. The QE ratios provide a useful method for evaluating the various bandgap designs, and several examples of this technique are included in chapter 4.

3. Urbach Energy

As outlined in chapter 1, the Urbach energy is one measure of material quality since it closely follows the energy slope of the valence band tail states.[10] To determine the Urbach energy of the alloys, a series of devices were made with all the same i-layer thicknesses and only had bandgap grading at the p-i interface. These devices had

systematically increasing germanium contents and temperature variations to cover the range of possible optimized device deposition conditions.

The Urbach energy is found from a log plot of the QE(λ) values at zero voltage and long wavelength. The long wavelength photons (800 nm $< \lambda <$ 1000 nm) are absorbed by the band tails with the absorption coefficients of equation 1.2. Rearranging equation 1.2 shows that the inverse of the slope on the log plot of the QE will provide an estimate of the Urbach energy. High-quality a-Si:H usually has Urbach energy values of around 45-47 meV.[10] Alloying always results in an increase in the Urbach energy, with values reaching 50-60 meV, depending on alloy content.[22] There has been some debate in the literature on whether the Urbach energy will always change with alloying, or if there is a lower limit that has not yet been found. Several reports have indicated that 50 meV is the best value for any silicon-germanium alloy that can be achieved, independent of germanium content.[19] The Urbach energies found during this work indicate that lower values can be reached with improved deposition conditions, and that the energy increases with increasing germanium content.

4. Tauc Gap

The log plot of the long wavelength QE(λ) used for the Urbach energy measurement can also be used to estimate the Tauc gap. An example of this measurement technique is shown in Figure 3.4. If the Tauc gap of an intrinsic material is known, and the material is incorporated into the i-layer of a constant bandgap device, then its long wavelength QE(λ) plot can be used as a reference for samples where the Tauc gap is not known.

Since the absorption by the band tails begins when the photon energy drops below the Tauc gap, the plot of QE(λ) will drop off at the Tauc gap energy. Then, determining the Tauc gap of an unknown sample is accomplished simply by measuring

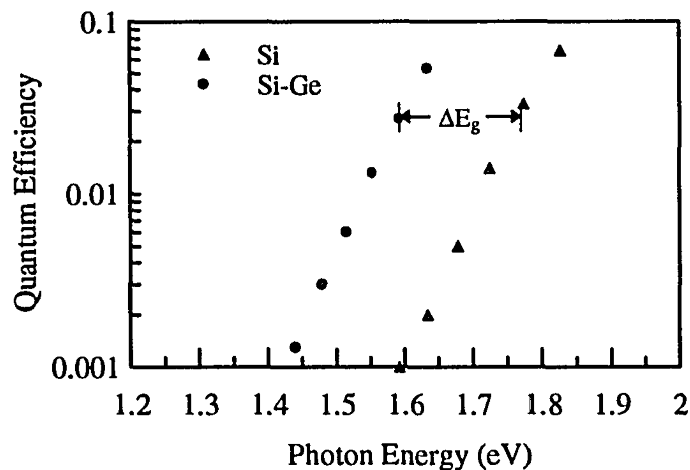

Figure 3.4. Example of the subgap quantum efficiency for a constant bandgap device; the inverse of the slope is the Urbach energy and the energy shift provides an estimate of the Tauc gap for the unknown sample

the shift in energy (ΔE_g) of the QE(λ) plots compared to the known sample. All of the constant bandgap devices used for this measurement were fabricated with similar deposition parameters, while only the gas flow rates and substrate temperatures changed.

C. Modeling

A detailed discussion on the background of a-Si:H modeling can be found in this author's master's thesis, including the description of a new method of modeling p-i-n devices.[15] The model is used here to guide the design of optimized device structures. The model is also expanded to include new device measurement techniques, and a brief description of the model will be presented here.

The model uses a greatly simplified algorithm for finding the internal electric fields in the device structures for various biasing levels and bandgap designs. It has proven to be more useful than more complex programs such as the AMPS program produced by Penn State. In particular, the AMPS program does not allow the user to study different forms of output such as the electric field profile at different levels of bias voltage. The program used for this work will allow the determination of the hole transport parameters, and the program successfully predicts which device designs will have greater efficiency. Also, the program is versatile enough to accommodate the non-uniform transport properties and defect densities found in a graded gap i-layer.

The simulation of photogenerated carrier collection begins by finding the fixed charge density as a function of distance into the i-layer by integrating the defect density over the energy shift created by band bending

$$\rho(x) = qg_o \int_{E_f}^{E} \exp\left(\frac{E'}{E_a}\right) dE' + qN_t \tag{3.6}$$

using the energy-dependent density-of-states equation

$$g(E) = g_o \exp\left(\frac{E}{E_a}\right) \tag{3.7}$$

The density of states modeled by equation 3.7 is the deep level defect density between the band tails shown in Figure 1.3. The initial defect density g_o, energy slope E_a, and midgap charge density N_t can be determined using the model as described later in this section.

The deep level defects are assumed to be charged when they cross the Fermi level as the bands bend. This approximation results in an occupation probability error on the order of kT/qE_a, which is small since E_a is normally greater than kT/q by a factor of four or more. The band bending in the i-layer is created by the doped p- and n-layers above and below the i-layer. The extent of the band bending depends on the density-of-states distribution described by equation 3.7. Biasing the device will also alter the band bending, which is an important effect included in this model that is neglected in other models such as AMPS.

From the fixed charge distribution found with equation 3.6 and using Poisson's equation, the electric field $\mathcal{E}(x)$ at any position x can be found from

$$\mathcal{E}(x) = \sqrt{\frac{2g_0E_a^2}{\epsilon}\left[\exp\left(\frac{qV(x)}{E_a}\right)-1\right]+\frac{2q}{\epsilon}\left[N_tV(x)-g_0E_aV(x)\right]+\mathcal{E}_0^2} \tag{3.8}$$

where $\mathcal{E}_o$ is found by the model. Since the voltage V(x) also varies with position, it must be found first by using the identity $d\mathcal{E}/dx = \mathcal{E}d\mathcal{E}/dv$ and integrating the equation

$$x = \int_0^{V_f} \frac{dV}{\mathcal{E}(x)} \tag{3.9}$$

where the right-hand side of equation 3.8 is substituted into the integral for $\mathcal{E}(x)$. Equation 3.9 is solved numerically for V(x) using a Simpson's rule quadrature method. This simple method easily allows the inclusion of other x-dependent variables and makes this method very versatile. The value of g_o will depend on the germanium concentration, so it too will vary with position x in a graded gap cell. Also, the upper limit for the integral V_f can be easily changed to reflect changes in cell bias. Once V(x) is known, it can be substituted back into equation 3.8. Then, this electric field profile is used to determine hole drift in the i-layer.

Only hole transport and collection are considered in the model since the hole mobility is lower than the electron mobility in a-Si:H by approximately one order of magnitude, and therefore holes are the limiting carrier in determining the

photogenerated current. The kinetics of hole transport are simulated using the field-assisted diffusion formulation of Smith.[16] An effective diffusion length, known as the downstream diffusion length L_d, can be found from

$$\frac{1}{L_d} = \frac{1}{2L_p}\left[\left(\frac{\mathcal{E}}{\mathcal{E}_c}\right)^2 + 4\right]^{1/2} - \frac{\mathcal{E}}{2L_p\mathcal{E}_c} \qquad (3.10)$$

where L_p is the zero-field diffusion length, and $\mathcal{E}_c$ is a critical field defined by the relation

$$\mathcal{E}_c = {kT}/{qL_p} \qquad (3.11)$$

The zero-field diffusion length will change with alloy content in a graded gap cell, so L_p is also a function of position x within the i-layer. L_p is related to the carrier mobility-lifetime product $\mu\tau$ by

$$L_p = \sqrt{\mu\tau\frac{kT}{q}} \qquad (3.12)$$

Once the effective diffusion length is known for every position x, hole transport can be found from

$$\Delta p(x) = \Delta p_o \exp\left(\frac{-x}{L_d}\right) \qquad (3.13)$$

where Δp_o is the photogenerated hole density at any position within the i-layer and $\Delta p(x)$ is the hole density at any distance x from that point. This formulation for hole transport is a very effective method for accommodating the non-uniform electric fields found in the p-i-n diodes. Under forward bias conditions, some i-layer configurations result in regions of zero electric field near the center of the diode. Then, holes are transported solely by diffusion, and L_d reduces to L_p.

Generally, the transport properties for a-Si:H are reported in terms of the mobility-lifetime product $\mu\tau$. The hole $\mu\tau$ product is of particular interest for a-Si:H and its alloys since the photogenerated holes are the limiting carrier in solar cell diodes. The model presented here provides a method for estimating this important parameter for alloys under device conditions.

The collection of photogenerated holes can be quantified in devices by measuring the current while the cell is illuminated. Therefore accurate modeling of the current provides an estimate of the internal electric fields and transport parameters. In particular, the QE(λ,V) ratios discussed previously provide a sensitive probe of the device properties. The method for estimating the hole $\mu\tau$ and the electric field profile is discussed next.

Holes are generated in the i-layer according to the rate equation

$$G(\lambda) = G_0(\lambda)\alpha(\lambda)\exp\{-\alpha(\lambda)x\} \qquad (3.14)$$

where $G_o(\lambda)$ is the incident photon flux at wavelength λ, and $\alpha(\lambda)$ is found from equation 1.1. Using equations 3.13 and 3.14, the internal QE(λ,V) can be found from the integral

$$QE(\lambda, V) = \int_0^L G(\lambda) \exp\left(\int_0^x \frac{-dx'}{L_d(x', V)} \right) dx \tag{3.15}$$

where L is the total thickness of the i-layer. The hole transport from the point of hole generation to the p-layer is found using the exponent inside the integral of equation 3.15. The exponential term is also an integral since the effective diffusion length is not a constant value in the i-layer as seen by equations 3.10 and 3.12, and must be integrated over the path of hole motion. How well the numerical evaluation of equation 3.15 reproduces experimental results depends primarily on the accuracy of the electric field simulation and on the estimate of the hole transport parameter $\mu\tau$.

Since the quantum efficiency depends on both the cell bias voltage and the incident photon wavelength, experimentally varying both over a range of values provides a wide variety of cell conditions. Then, an accurate simulation of the experimental values over the entire range of wavelengths and bias voltages would indicate that the transport parameters and electric field profiles used in the model are also accurate. Also, the value for the $\mu\tau$ product found from the simulation would

provide valuable new information about the silicon-germanium system. This parameter is very useful for determining the dimensions and alloy content of an optimized device structure. Also, a reasonable estimate of the midgap state parameters g_o, E_a and N_t can be extracted from the modeling since they play a role in determining the electric field profile.

D. Device Optimization

Once the a-Si:H and alloyed material are fully characterized using the methods described above, the model is used to guide the design of an optimized graded gap structure. A multiple bandgap grading scheme is needed to make full use of the available interface electric fields and still have an adequate field near the center of the cell. The low bandgap region should have a high germanium content to maximize low-energy light absorption, but not so high that it inhibits hole collection. The device optimization process is described in detail in chapter 4, along with the final bandgap design found for this project.

The criteria that was used in both the modeling and the experimental work to optimize the cells is the long wavelength QE. The germanium content at every position in the i-layer, as well as the overall thickness of the i-layer, were varied in the model to determine a starting point for the experimental work. Then, the final optimized device structure was determined from the experimental QE and I(V) results.

IV. RESULTS

A. Material Quality

1. Film Characteristics

To determine the quality of the alloyed material and the parameters to use in the computer modeling, a series of a-(Si,Ge):H films were grown with the deposition conditions listed in Table 4.1. A large number of pure a-Si:H films have been grown in the PECVD reactor by previous workers at this facility, and the parameters that produce a typical high-quality film were used for sample #1/300 listed in the table. This was one of many films grown to compare the properties of the pure a-Si:H with the a-(Si,Ge):H alloys during this work and is included here for comparison.

The electrical and optical characteristics of these films are listed in Table 4.2. The Tauc gap energies are found from Tauc plots as shown in Figure 3.1. The activation or fermi energy values all were near the center of the Tauc gap with the exception of sample #1/305. The low activation energy for sample #1/305 indicates that it has higher levels of impurities, while all of the other films were more nearly intrinsic. The most likely source for the impurities in #1/305 was the substrate cleaning step, since the chamber base pressure is monitored for leaks before and after a run. Also, this sample was made in the middle of a series of intrinsic runs, and no dopant impurities

Table 4.1. Deposition conditions of a-(Si,Ge):H films used for optical and electrical characterization

Sample #	Pressure (mTorr)	Temp (°C)	Time (min.)	Power (watts)	Vsub (volts)	Gas Flow Rates 100% SiH_4 (sccm)	10% GeH_4 (sccm)	100% H_2 (sccm)
1/300	20.9	350	180	25	0	4	0	40
1/303	19.0	300	180	22	-30	8	8	50
1/304	19.6	300	210	22	-30	10	6	52
1/305	19.9	300	210	22	-30	8	12	50
1/306	19.8	350	205	22	-30	8	12	50
1/307	22.0	350	210	22	-30	6	3	60
1/308	19.4	350	270	22	-30	10	6	52
1/309	22.0	300	310	22	-30	6	8	60
1/310	17.2	350	270	25	-30	8	8	50
1/311	20.1	350	270	26	-30	8	12	50
1/312	22.1	350	300	23	-30	6	8	60

appeared in the samples deposited before and after #1/305, indicating that the chamber was not contaminated.

The growth rates listed in Table 4.2 are highly consistent, with small increases at increased plasma power levels and small decreases with higher levels of hydrogen dilution. Hydrogen dilution is known to lower the growth rate by reducing the mean free path of the reactive SiH_x molecules and by etching the sample surface.[24] This

Table 4.2. Material characteristics

Sample #	Thickness (μm)	Tauc gap (eV)	Act. energy (eV)	σ_d (S/cm)	σ_{ph} (S/cm)	Photosens. (σ_d/σ_{ph})	Growth rate (Å/s)
1/300	0.63	1.78	0.82	8.7e-05	2.0e-10	4.4e+05	0.58
1/303	0.61	1.59	--	7.4e-06	1.7e-10	4.4e+04	0.56
1/304	0.68	1.62	0.8	1.9e-05	6.1e-11	3.1e+05	0.54
1/305	0.68	1.47	0.5	1.4e-05	2.2e-09	6.4e+04	0.54
1/306	0.66	1.46	0.69	4.5e-06	6.0e-10	7.5e+03	0.54
1/307	0.55	1.52	0.75	7.3e-06	1.8e-10	4.1e+04	0.43
1/308	0.84	1.63	--	1.5e-05	5.0e-11	3.0e+05	0.52
1/309	0.8	1.54	0.74	5.5e-06	1.7e-10	3.2e+04	0.43
1/310	0.8	1.56	--	6.3e-06	9.4e-11	6.7e+04	0.63
1/311	0.88	1.47	--	3.2e-06	4.1e-10	7.8e+03	0.54
1/312	0.77	1.55	--	6.8e-06	1.8e-10	3.9e+04	0.43

surface etching is beneficial since weakly bonded silicon is removed before it becomes incorporated into the material.

The photosensitivity values listed in Table 4.2 decrease somewhat with increasing germanium content. This result is expected since the germanium introduces new midgap defects that reduce the photogenerated carrier lifetimes. Also, the dark conductivity will increase with decreasing Tauc gap as shown by equation 3.3. The

drop in photosensitivity is not severe, which provides the first indication that the silicon-germanium films are device quality.

Previous photosensitivity data reported in the literature indicate that a-(Si,Ge):H films can have a wide range of values for the photo- and dark conductivity. Both parameters often vary over several orders of magnitude at a particular value for the germanium content. The dependence of the dark and photoconductivity on the Tauc gap for the films in Table 4.1 is shown in Figure 4.1. The consistent results obtained indicates that high quality material can be deposited on a reproducible basis.

Another indication of material quality is the value of the absorption coefficient at photon energies below the Tauc gap energy. Photon absorption in this subgap energy

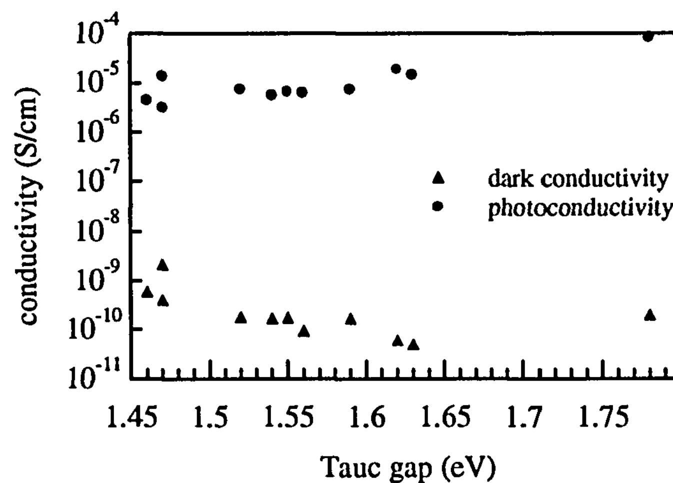

Figure 4.1. Photo- and dark conductivity dependence on Tauc gap for the a-(Si,Ge):H films

range is due to the presence of energy states within the Tauc gap. Low values for the absorption coefficient ($\leq 3.0\ cm^{-1}$) are indicative of low defect densities. The absorption coefficient used for this measurement is found from the knee of the absorption data from the a-(Si,Ge):H films and is shown in Figure 4.2. The results indicate that the midgap defect density does increase with germanium content, but the values are within device quality range.

To determine how the Tauc gap and other material parameters change with germanium content, a series of films were prepared for EDS analysis. The film series contained both flow rate variations and temperature variations as shown in Table 4.3. One sample, #1/821, was deposited on a glass substrate, while the rest of the samples were deposited on conducting tin-oxide substrates to simulate device deposition

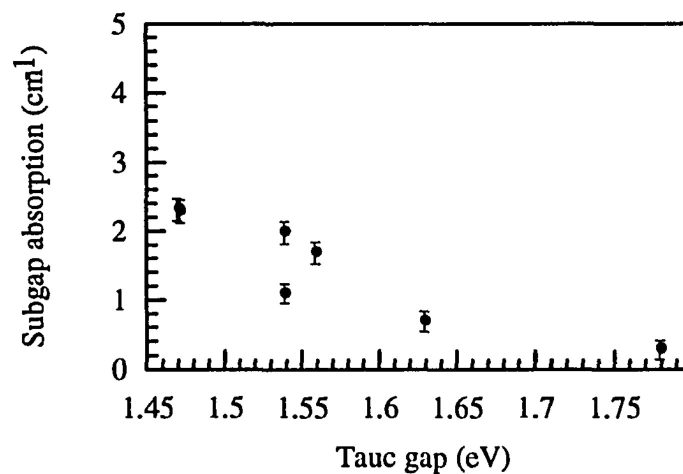

Figure 4.2. Subgap absorption coefficient dependence on Tauc gap energy

conditions and to prevent charging effects in the film from the incident electron beam.

The EDS spectra for samples #1/822, #1/826 and #1/827 are shown in Figure 4.3. These samples had varying germane and silane flow rates and constant substrate temperatures as listed in Table 4.3. This series of films was deposited to determine the germanium content in the material as a function of germane gas flowing into the chamber. This measurement is important for the graded bandgap devices since they will be fabricated by varying the flow ratios of the process gases during the i-layer deposition. The EDS characteristic x-ray emission peak at 1200 eV is the germanium Lα peak and the peak at 1735 eV is the silicon Kα peak. The spectra shown in Figure 4.3 are of the unanalyzed raw data from the x-ray detector, and indicate that any impurities in the samples are present only at low concentrations, since no other

Table 4.3. Deposition parameters of a-(Si,Ge):H films for EDS analysis

						Gas Flow Rates		
Sample #	Pressure (mTorr)	Temp (°C)	Time (min.)	Power (watts)	Vsub (volts)	100% SiH_4 (sccm)	10% GeH_4 (sccm)	100% H_2 (sccm)
1/821	18.0	300	180	22	-40	2	10	40
1/822	18.0	300	180	23	-40	2	10	40
1/826	18.2	300	180	21	-40	4	8	40
1/827	20.9	300	180	22	-40	2	16	40
1/828	18.2	250	180	22	-40	2	10	40
1/829	18.0	350	180	23	-40	2	10	40

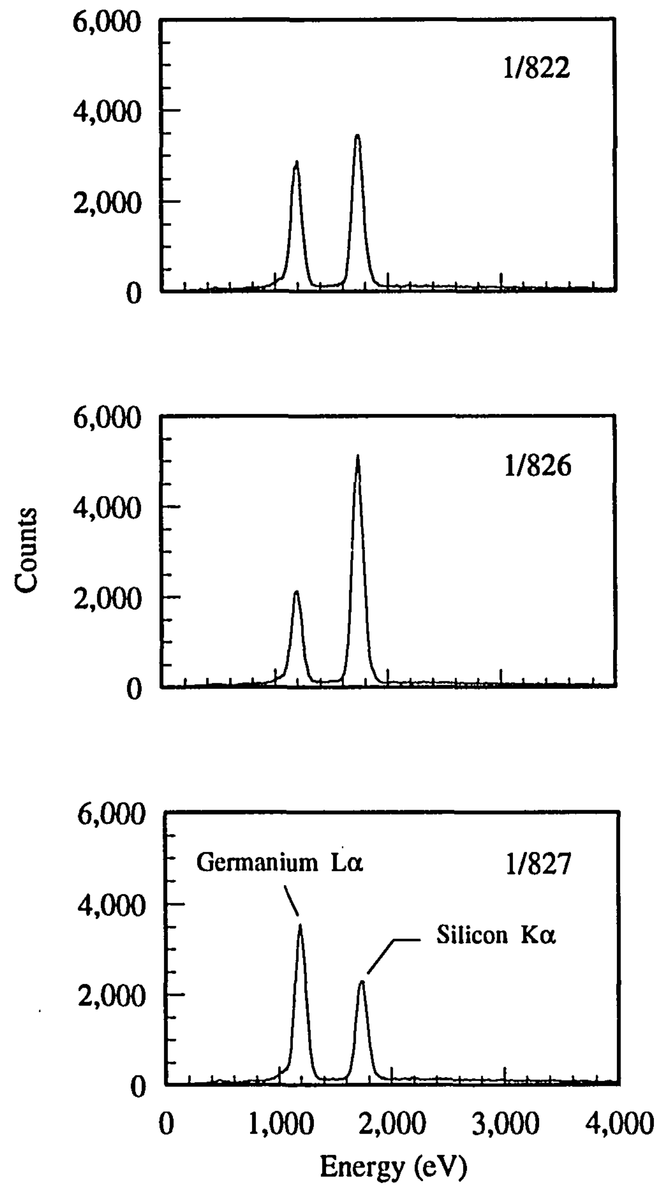

Figure 4.3. Energy dispersive x-ray spectra of the a-(Si,Ge):H samples

peaks are seen in the spectra. The x-ray detector has a low-absorption thin window that allows the detection of the characteristic x-rays from elements beginning with boron and continuing on to the heavier elements. Therefore, impurities such as oxygen would be detected and the absence of an oxygen peak in the spectra indicates that it is present only in quantities smaller than two to three atomic percent.

The relative intensities of the peaks are related to the silicon and germanium content. An estimate of the concentration of silicon and germanium in the films is made using the peak intensity, the x-ray signal from pure a-Si:H and pure a-Ge:H standards and the computer program supplied with the Kevex detector. Atomic mass, absorption and fluorescence corrections (ZAF) are made automatically by the program.

The silicon and germanium concentrations found in the films using EDS are listed in Table 4.4. Sample #1/821, which was deposited on a glass substrate, had a large variation in count rate from the center to the edge of the sample. The x-ray counts from the edge of this sample were taken with the incident beam in close proximity to the carbon paint grounding contact, indicating that the low count rate from the center region was most likely due to charging effects.

All of the other substrates were conducting tin-oxide, which showed no charging effects and good spatial uniformity across the films. To determine if the substrate itself had any effect on the film composition, sample #1/822 was prepared with identical

Table 4.4. Alloy percentages and EDS peak count rates

Sample #	Location	Silicon atomic %	Germanium atomc %	Silicon Kα (counts/sec)	Germanium Lα (counts/sec)
1/821	center	62.8	37.2	157	147
	edge	64.8	35.2	265	227
1/822	center	66.1	33.9	299	241
	edge	65.8	34.2	295	242
1/826	center	78.9	21.1	438	177
	edge	79.6	20.4	448	173
1/827	center	51.4	48.6	194	297
	edge	51.6	48.4	200	305
1/828	center	65.5	34.5	299	248
	edge	65.7	34.3	287	238
1/829	center	66.0	34.0	306	250
	edge	66.3	33.7	317	255

deposition parameters as #1/821. The germanium content for these two films is the same within the experimental error of ~10%, indicating that the substrate has very little effect on the composition. This test was important since the growth rate was observed to increase for films deposited on tin-oxide, which may have resulted in altered composition.

A linear relationship is found between the atomic percent of silicon and germanium that is incorporated into the amorphous network and the mass flow ratio of silane and germane gas into the reactor chamber. This relationship is shown in Figure

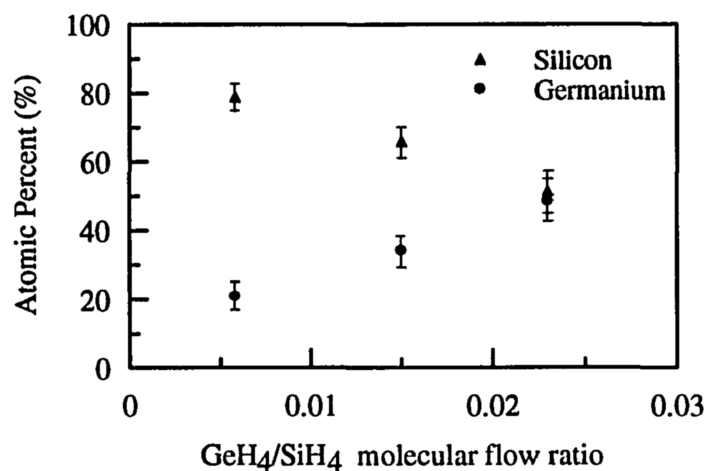

Figure 4.4. The relationship between the incorporation of silicon and germanium into the amorphous network and the germane to silane molecular flow ratio into the reactor chamber

4.4, and is used to estimate the germanium concentration for all of the alloy depositions.

Figure 4.4 also shows that a large percentage of the germanium flowing into the chamber as GeH_4 gas is incorporated into the films, as compared to silicon from the SiH_4 gas. This is consistent with the fact that the germanium-hydrogen bonds are weaker than the silicon-hydrogen bonds and are more easily broken by the energetic species within the plasma. This may also be a contributing factor to the heterogeneity sometimes found in the a-(Si,Ge):H films, since the germanium may be incorporated into the films as fast as it flows into the chamber.

The germane to silane flow ratio was the same in samples #1/822, #1/828 and #1/829 and all were deposited on tin-oxide substrates. The only variation in these three films was the substrate temperature, as shown in Table 4.4. The variation in germanium content with substrate temperature is minimal and well within the experimental error. This result indicates that no thermally activated germanium growth is occurring up to 350 °C during the deposition process.

With the EDS results, the other material parameters can be correlated with the alloy composition. The Tauc gap results listed in Table 4.2 are plotted versus germanium content in Figure 4.5 below. A linear fit to the data results in the equation

$$E_g(eV) = 1.79 - 1.2x \tag{4.1}$$

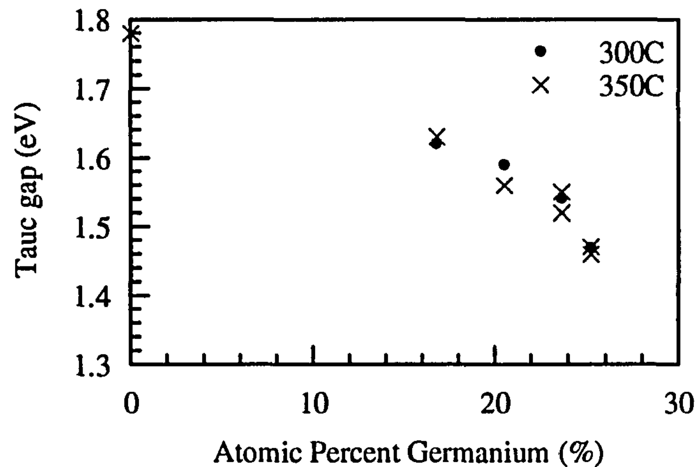

Figure 4.5. Relationship between Tauc gap energy and germanium content in the films

where x is the atomic germanium concentration in a-$Si_{1-x}Ge_x$:H. The slope is somewhat steeper than what is reported in the literature, but the Tauc gap results are also dependent on film thickness, which may have introduced some error into these results.

The final analysis of film quality presented here is transmission electron microscopy. As explained in chapter 3, the substrates for TEM are carbon coated copper grids that are 3 mm in diameter. The films are deposited directly on these substrates, which are then loaded into the microscope. The film deposition parameters for TEM are listed in Table 4.5.

Table 4.5. Deposition parameters of a-(Si,Ge):H films for TEM analysis

						Gas Flow Rates		
Sample #	Pressure (mTorr)	Temp (°C)	Time (min.)	Power (watts)	Vsub (volts)	100% SiH_4 (sccm)	10% GeH_4 (sccm)	100% H_2 (sccm)
1/410	15.8	250	11	26	0	8	0	0
1/415	19.5	350	16	22	0	5	6	52
1/416	20.2	300	16	22	0	4	12	50
1/417	20.8	300	30	22	0	4	12	50
1/421	20.4	250	22	22	0	4	12	50
1/422	20.0	250	20	19	-30	4	12	50
1/423	20.1	350	20	19	0	4	12	50
1/424	20.0	300	20	19	-30	4	12	50

The film series includes a range of substrate temperatures as well as zero and negative substrate bias voltages to study the effects of induced ion bombardment. It is expected that higher substrate temperatures will increase the surface mobility of the incident ions and radicals and promote the growth of a more homogenous network. The induced ion bombardment should have a similar effect since the incident ions provide excess energy to the growing surface. All of the films were deposited with the same gas flow rates except for one high temperature film that had a lower germane flow rate and one pure a-Si:H film.

Diffraction patterns from all of the films consisted solely of rings for all incident beam locations and angles, verifying that the material is amorphous. Also, the pattern of the rings from the films was different from the pattern of a bare carbon substrate indicating that the images are of the alloyed material. A typical diffraction pattern is shown in Figure 4.6. The micrograph shown in Figure 4.7 is of film #1/421, which was a low temperature film with no substrate bias. The visible contrast indicates that some form of heterogeneity is occurring with these deposition conditions. The pure a-Si:H film #1/410, which was deposited at the same low temperature, was entirely homogenous with no visible contrast down to the resolution of the microscope. The magnification of the image from the microscope and from the photographic enlargement for all of the micrographs shown in the figures is 1,600,000x.

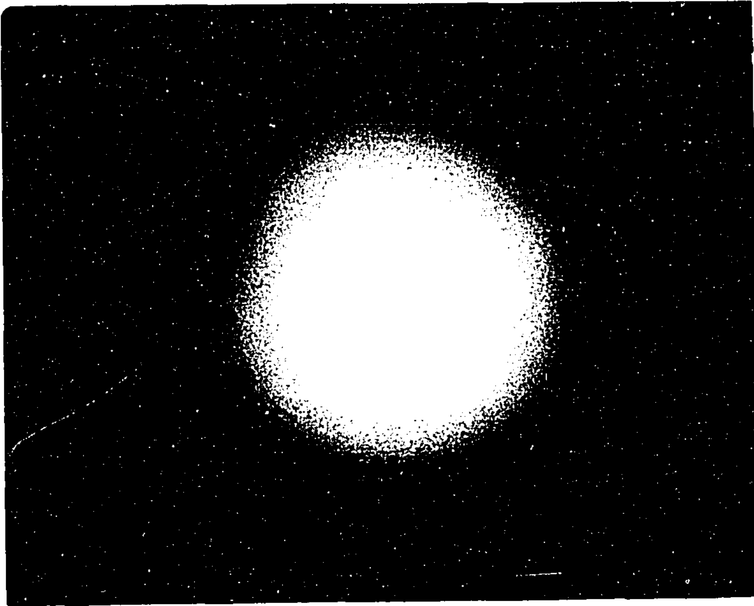

Figure 4.6. Typical diffraction pattern of the a-(Si,Ge):H TEM samples

Figure 4.7. TEM image of sample #1/421 deposited at 250 °C and V_{sub}=0V

The a-(Si,Ge):H film #1/416 was deposited at 300 °C with the substrate bias (Vsub) at zero volts. Contrast is seen in the micrograph image of this film shown in Figure 4.8, but in smaller regions. The same is true for film #1/417 shown in Figure 4.9, which was deposited with the same parameters as #1/416 but with a longer deposition time. This film was grown to determine the effect, if any, of film thickness on the micrograph image. There does not appear to be any thickness effects on the microstructure. From these two films, it appears that the high temperature deposition consistently produces higher quality material.

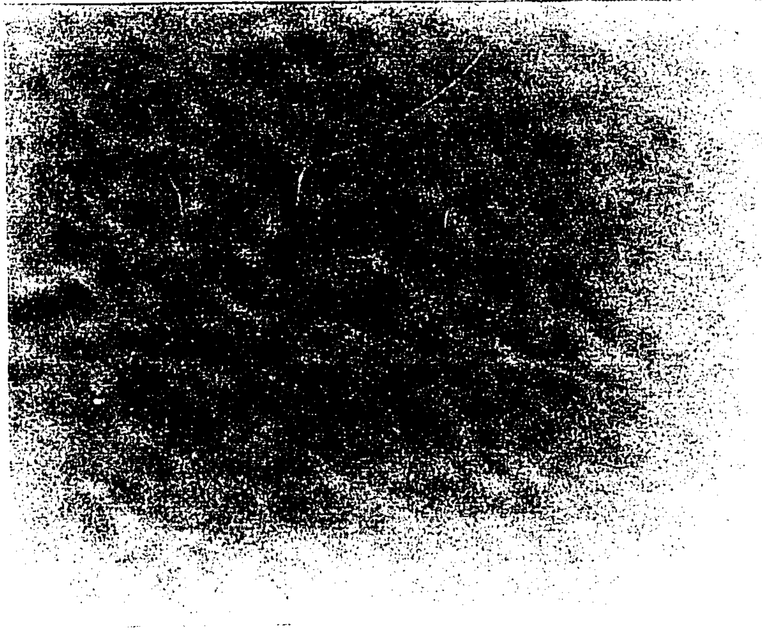

Figure 4.8. TEM image of sample #1/416, deposited at 300 °C and V_{sub}=0V

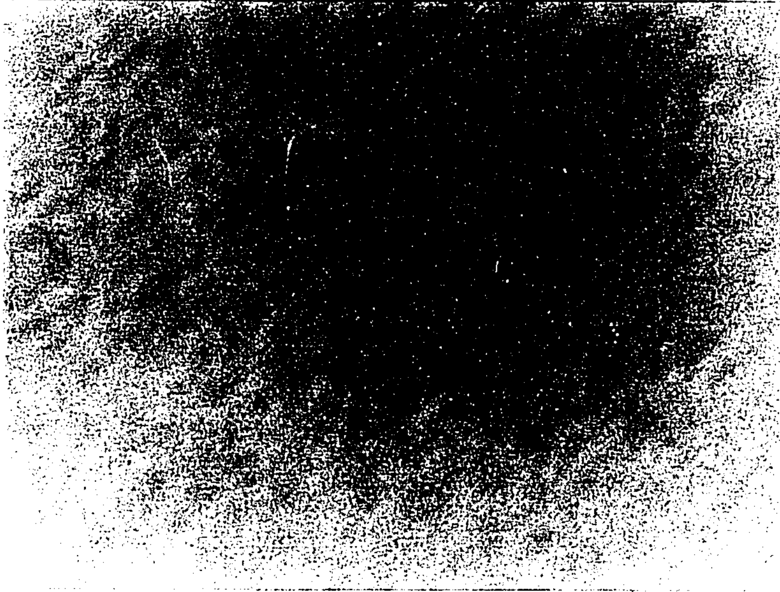

Figure 4.9. TEM image of sample #1/417, which was deposited with the same parameters as #1/416 but is approximately twice as thick

The final micrograph image, shown in Figure 4.10, is of film #1/422, and shows the effects of substrate bias on the low temperature films. Again, the regions of contrast are smaller in size indicating a higher degree of homogeneity. It appears that the induced ion bombardment does improve the quality of the alloy. The other films, #1/415, #1/423, #1/424, all had no visible contrast. The results of the TEM analysis correlate well with the electronic data, which also show that the best materials are deposited at higher temperatures and that a negative substrate bias improves the quality of the alloyed material.

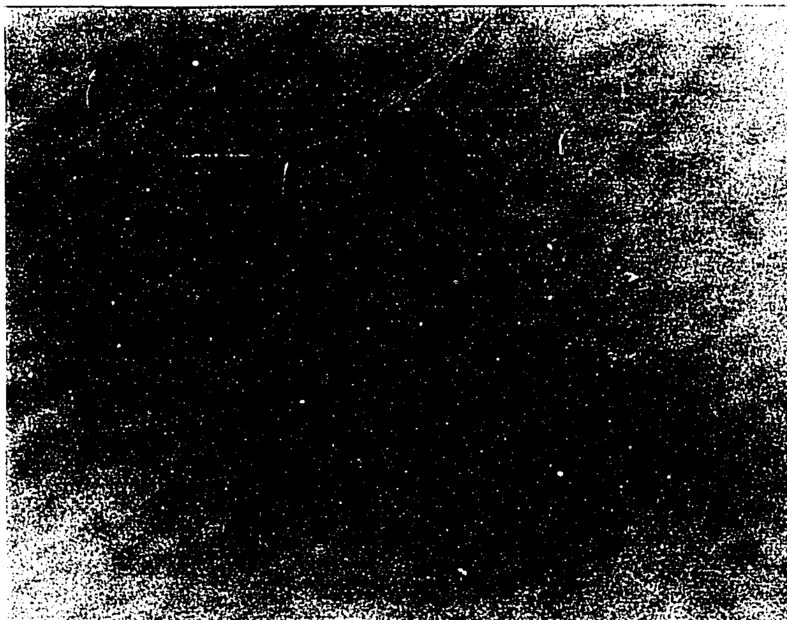

Figure 4.10. TEM image of sample #1/422, deposited at 250 °C and V_{sub}= -40V

Another parameter that can be used to characterize the films is the absorption coefficient prefactor B from equation 1.1. This parameter is especially useful for the computer model to ensure that the proper absorption coefficient is used for each level of germanium content. Figure 4.11 shows that the value of B decreases with Tauc gap energy. This result is expected since the germanium used to lower the Tauc gap also increases the slope of the band tails, which plays a role in determining B as seen in equation 3.5. The deposition conditions other than gas flow rates may also play a role

in the value of B creating the scatter seen in the graph, but there does not appear to be a strong correlation between deposition temperature and B in Figure 4.11.

2. Constant Bandgap Devices

P-i-n devices with constant bandgap i-layers are also used to study material quality as outlined in chapter 3. Quantum efficiency results in particular provide a great deal of additional information about the material quality. An added advantage of device characterization is that the material parameters are measured under the same deposition and device operating conditions as the final optimized devices. The most important of these conditions include the internal electric field in the i-layer, and the

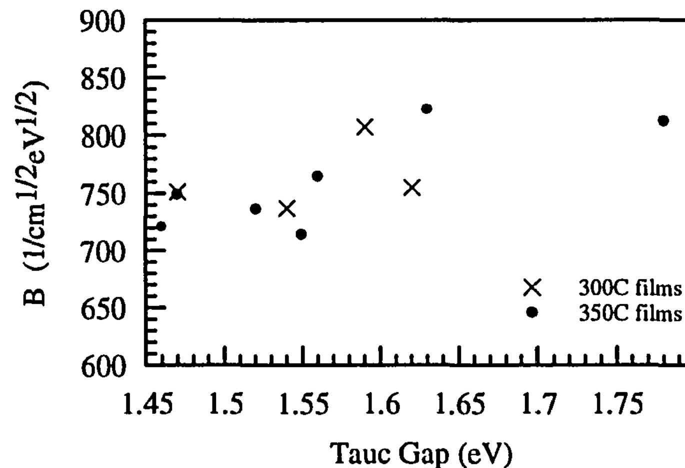

Figure 4.11. Relationship between the absorption coefficient prefactor B and the Tauc gap energy

presence of dopant atoms from the p-layer deposition. Also, new information can be obtained about material quality with the device structures and the results of the computer model, as outlined next.

The series of device depositions is extensive since the conditions for producing the highest quality material for devices were unknown. Each of the improvements in device quality led to new deposition regimes, and extended the device series. A series of varying bandgap i-layers were grown once the optimum deposition parameters were found. A complete list of all of the device deposition parameters is included in the Appendix, and the results are summarized next.

The Tauc gap results found by measuring the shift in absorption edge for the all of the devices deposited at 300 °C are shown in Figure 4.12. Also included in the figure are the results from the 300 °C films using the Tauc plot method. Good correlation is obtained between the two different bandgap measurement methods. The linear relationship between germanium content and energy gap has a slightly shallower slope for the devices as compared to the films (see equation 4.1). The equation found for a linear fit to the device data of Figure 4.12 is

$$E_g(eV) = 1.76 - 0.9x \tag{4.2}$$

with x as the germanium atomic fraction. This relationship is close to that reported in the literature by other groups using similar deposition parameters.

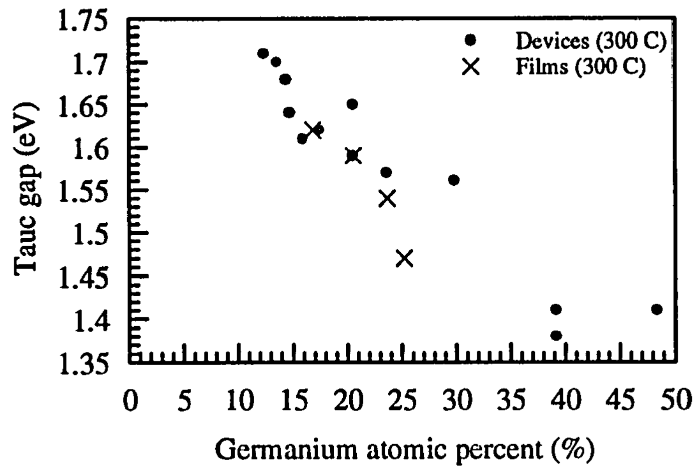

Figure 4.12. Device and film Tauc gap variation with germanium content

The Tauc gap data for all of the constant bandgap devices is plotted in Figure 4.13. As with the film results, there does not appear to be a strong correlation between bandgap and substrate deposition temperature for the devices deposited at 300 °C and 350 °C. There does appear to be a small increase in Tauc gap energy for the films deposited at 250 °C. This result indicates that adequate levels of hydrogen for passivating the dangling bonds are maintained at the higher deposition temperatures.

A decrease in the measured Tauc gap for the higher temperature films would have indicated that the hydrogen content was reduced. The hydrogen content apparently increases somewhat for lower deposition temperatures, and may contribute to the

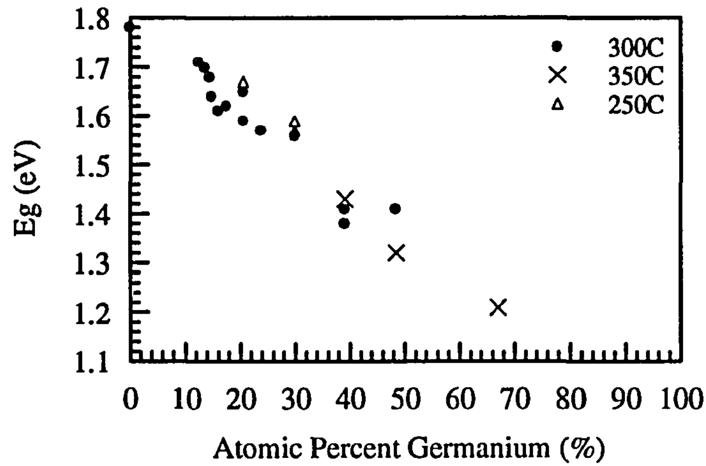

Figure 4.13. Tauc gap dependence on germanium content in constant bandgap i-layer devices

lower material quality seen for these films by introducing new defects in the microstructure such as hydrogen-rich voids.

The results thus far have consistently indicated that the conditions for depositing high quality amorphous silicon-germanium include elevated substrate temperatures (at least 300 °C), high levels of hydrogen dilution and a negative substrate bias voltage. These conditions are different than what is used to deposit pure amorphous silicon samples.

The next parameter that can be measured for the constant bandgap devices is the Urbach energy. As explained in chapter 3, this measurement is an indication of

material quality since the Urbach energy closely follows the slope of the valence band tail states.[10] Higher values for the Urbach energy indicate broader valence band tails and larger defect densities.

The Urbach energies for the constant bandgap devices are shown in Figure 4.14. Again, there does not appear to be a strong temperature dependence, although there is a small increase in the Urbach energy for the i-layers deposited at 250 °C, which agrees with the TEM and Tauc gap results indicating that higher quality material is deposited at higher substrate temperatures. The results of Figure 4.14 also clearly show that the Urbach energy does depend on germanium content. Previous reports have speculated that there is a constant value for the silicon-germanium Urbach

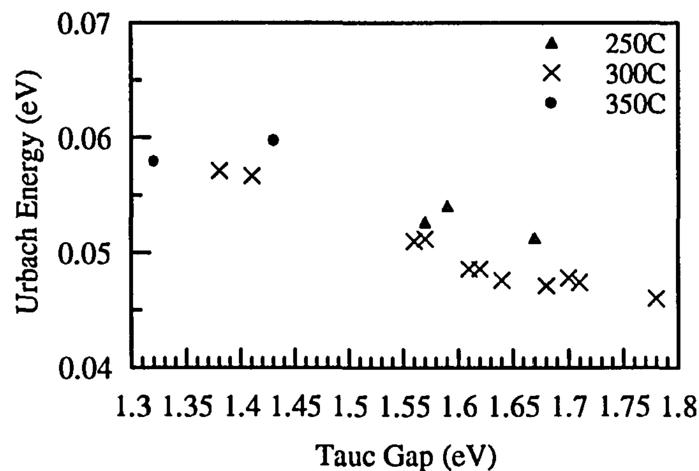

Figure 4.14. Urbach energy as a function of Tauc gap for the constant bandgap devices

energy, independent of alloy composition.[19] This constant value for the Urbach energy is usually estimated at 50 meV. The results shown in Figure 4.14 indicate that lower values for the Urbach energy can be attained, and that increasing the germanium content will increase the Urbach energy.

Another indication of material quality as outlined in chapter 3 is the hole mobility lifetime product $\mu\tau$. To determine a value for the $\mu\tau$ product in the constant bandgap devices, an accurate model of the internal electric field in the i-layer must be found. Then, using the experimentally determined values for the quantum efficiency, equation 3.15 (along with equation 3.12 to convert $\mu\tau$ to a diffusion length) is used to determine $\mu\tau$. The method used to determine the correct electric field profile and subsequently $\mu\tau$ is described next.

The first approximation for the electric field profile used in the model is a simple constant profile. A constant electric field throughout the i-layer can be approximated by

$$\varepsilon(x) = \frac{V_{oc} - V_a}{2L} \tag{4.3}$$

where V_{oc} is the open circuit voltage, V_a is the applied bias voltage and L is the length of the i-layer. The factor of two in the denominator is used to account for the large reduction in the electric field at the p-i and i-n interfaces due to the band tails.

Accordingly, this approximation is not expected to be very accurate near the interfaces.

When this approximation is used to compute the quantum efficiency, QE(λ,V), a fairly good fit is achieved as shown in Figure 4.15. The QE(λ,V) values at short and medium wavelengths are fit fairly well at reverse and low forward bias voltages. The constant electric field approximation breaks down for the long wavelength region and at the higher forward bias voltages. The long wavelengths will be absorbed more deeply in the i-layer than the shorter wavelengths, and as a result are more strongly influenced by the magnitude of the electric field throughout the i-layer. Small

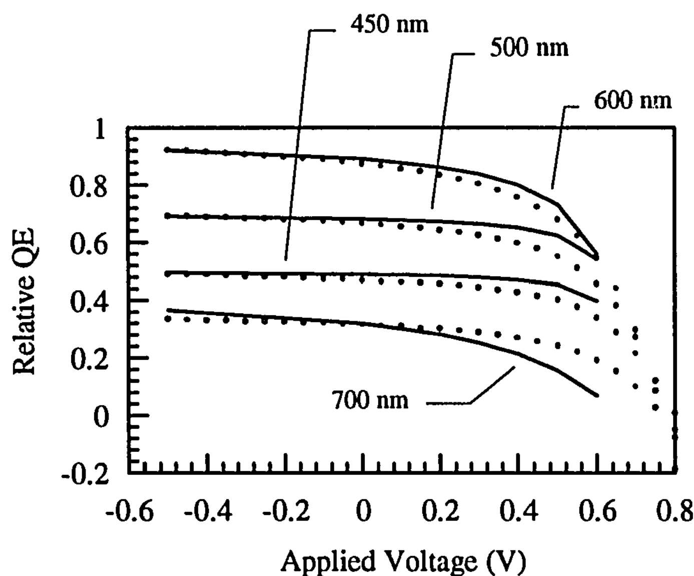

Figure 4.15. Constant electric field approximation (solid lines) for the quantum efficiency values (points) at four wavelengths from sample #1/536

deviations from the actual electric field profile will appear as a poor fit especially for the longer wavelengths, which is what appears in Figure 4.15.

Also, the strong forward bias region (≅0.5 V) is not well simulated for any of the wavelengths. The electric field in this region is reduced in the alloyed material more quickly than simulated by equation 4.3, due to the high density of states in the band tails. It is known that the electric field is actually highly non-uniform and may even reach a magnitude of zero near the center of the i-layer at forward bias, and then hole transport occurs by diffusion rather than drift. As a result, a more accurate electric field approximation is required to achieve a better fit to the QE(λ,V) curves.

When the electric field profiles from equation 3.8 are used to compute the QE(λ,V) values, a better fit for the long wavelength quantum efficiency values is achieved as shown in Figure 4.16. The electric field is highly non-uniform as shown in Figure 4.17, with high interface fields and low magnitudes near the center of the i-layer. Since the long wavelength QE curve is well simulated using this electric field profile, it is a much closer approximation to the actual profile than the constant field approximation.

From Figure 4.16, it appears that the strong forward bias region is again not well simulated by the field profile of Figure 4.17. The profile shown in Figure

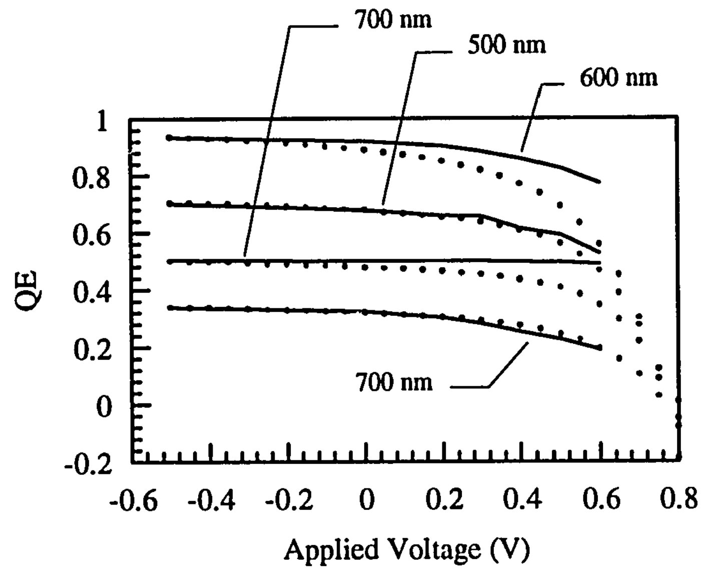

Figure 4.16. Non-uniform electric field approximation of sample #1/536

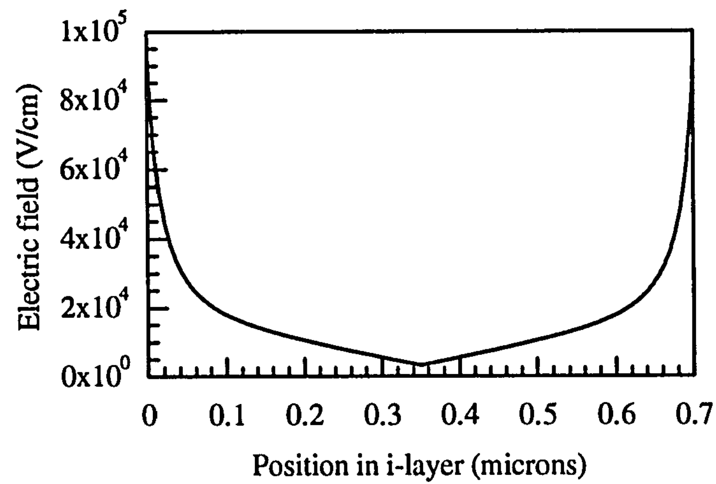

Figure 4.17. Simulated electric field profile in the i-layer at +0.5 volts for sample #1/536

4.17 is computed at +0.5 volts, and has high interface magnitudes. Since the QE values drop off more quickly than the simulated values, it appears that the interface fields are too high. Possibly, since the majority of the high energy photons are absorbed near the interface, there may be enough trapped charges at the interface to effectively lower the electric field.

When the field is reduced only at the p-i interface in the model, an excellent fit to the QE(λ,V) values are achieved as shown in Figure 4.18. To achieve this fit, the

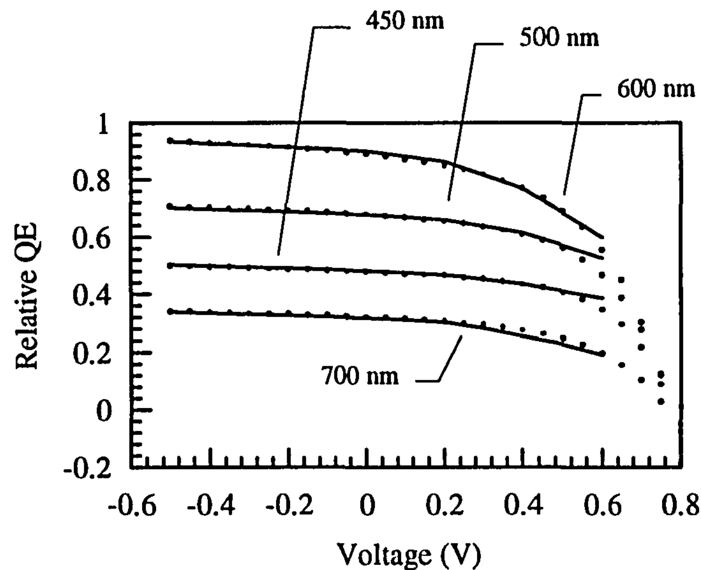

Figure 4.18. Non-uniform electric field approximation with reduced p-i interface fields for #1/536

magnitude of the field within 0.05 μm of the p-i interface was adjusted downward. The amount and extent of decrease in the electric field is dependent on the wavelength and applied voltage. This interface electric field then becomes the only other parameter besides the hole $\mu\tau$ product that is used to fit the QE curves shown in Figure 4.18.

Another possible indication why it is the interface electric field that must be adjusted is the dependence of open circuit voltage on the incident photon wavelength. This dependence, graphed in Figure 4.19, shows that the voltage increases with

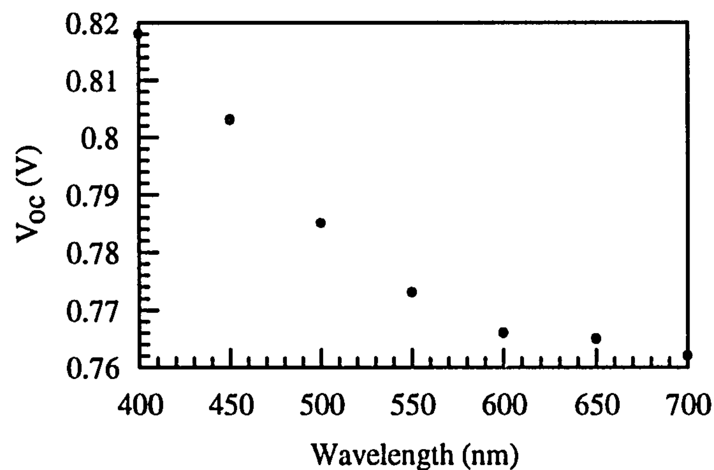

Figure 4.19. Dependence of the open circuit voltage on photon wavelength for a typical constant bandgap device

wavelength. The increase in voltage becomes more pronounced for wavelengths shorter than 600 nm, indicating that larger numbers of charges apparently are appearing at the p-i interface for these wavelengths.

The greater absorption coefficient for the shorter wavelengths may be the parameter that is responsible for the higher charge density at the interface. Whether this charge remains in the form of free carriers or whether it is due to a greater occupation probability for deep and shallow traps cannot be determined, but other researchers have reported evidence that the electric field is reduced at the interface that is nearest to the surface exposed to the incident photons.[20]

To summarize the results thus far, the simulated QE(λ,V) curves shown in Figure 4.18 were fit to the experimental data by adjusting three parameters. First, the absorption in the p-layer is found by setting the thickness and effective bandgap. The bandgap in the p-layer is not uniform since the temperature and carbon content are both varied throughout the p-layer deposition. A single effective bandgap is used in the model to simulate this region. The p-layer bandgap that best fit the devices with diborane as the p-layer dopant gas was 1.9 eV. The devices that used trimethylboron as the dopant gas required a larger effective p-layer bandgap of 2.0 eV.

The proper p-layer thickness and bandgap can be determined by matching the QE points from the model to the experimental points in the reverse bias region for all four of the wavelengths. As seen in Figure 4.18, the highest energy QE curve is the second

lowest curve on the graph. The p-layer absorbs a large portion of these photons reducing the QE. The QE curves increase in magnitude as the photon energy decreases since more photons pass through to the i-layer and contribute to the QE. Then, the 700 nm curve drops far down on the graph since these photons penetrate deep into the i-layer where the electric field is weak, or pass completely through the device and are not absorbed.

The model does allow for the reflection of photons off the back surface and reentry into the i-layer, but this is a fairly minor effect for the low levels of light used for the QE measurement. The reverse bias region is used to determine p-layer absorption since the electric field profile is at a maximum and the carrier collection does not depend as highly on the transport parameters, especially for the carriers generated by the high energy photon absorption.

Second, once the p-layer parameters are determined, the curvature of the QE values in forward bias can be simulated by setting the $\mu\tau$ for holes. Since the i-layer for these devices have a constant level of germanium, one value of $\mu\tau$ should fit all of the experimental data. Using all four wavelengths to determine the value of $\mu\tau$ is important since it provides greater accuracy and allows the separation of wavelength dependent effects such as the interface electric field magnitude, which is the third and final parameter used to fit the QE(λ,V) curves.

This method of approximating the hole $\mu\tau$ product allows the determination of this parameter to within an order of magnitude for the first time for a-(Si,Ge):H. The values for $\mu\tau$ found for the constant bandgap devices are plotted as a function of germanium content in Figure 4.20. This graph indicates that the alloyed material is of device quality up to a germanium concentration of about 25%. This level of germanium correlates to a Tauc gap of about 1.5 eV. Again, the 250 °C samples, with their low values of $\mu\tau$, have the poorest material quality. This ties in well with the results of all of the other material quality measurements, and indicates that the modeling is reasonably accurate.

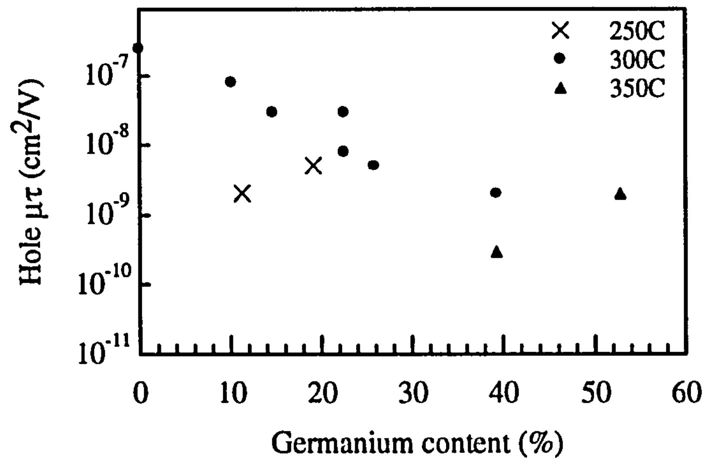

Figure 4.20. Hole mobility-lifetime product as a function of germanium content measured from the constant bandgap devices

Although it is primarily the defects created by adding germanium to the amorphous network that lowers the $\mu\tau$ product, other conditions present during deposition may contribute also. It is advantageous to look for another parameter that can be related to $\mu\tau$ that can be measured directly. Then, an estimate of the transport parameters can be made with this parameter rather than resorting to the lengthy modeling procedure.

The extent of the band tails should be affected by the germanium content and deposition conditions in the same way as $\mu\tau$, since the mobility is determined in part by the hole 'hopping' into and out of band tail states, which are created by disorder in the network. Since the Urbach energy provides a good estimate of the valence band tail, there should be a correlation between it and the $\mu\tau$ product. Figure 4.21 shows that there does appear to be a very good correlation. A numerical fit to the points in Figure 4.21 results in the equation

$$\mu\tau_h = \mu\tau_0 \exp\left[\frac{-E_\mu}{E_0}\right] \qquad (4.4)$$

where E_μ is the Urbach energy, E_o is the characteristic energy slope of ~3 meV, and $\mu\tau_o$ has a value of ~0.27 cm^2/V.

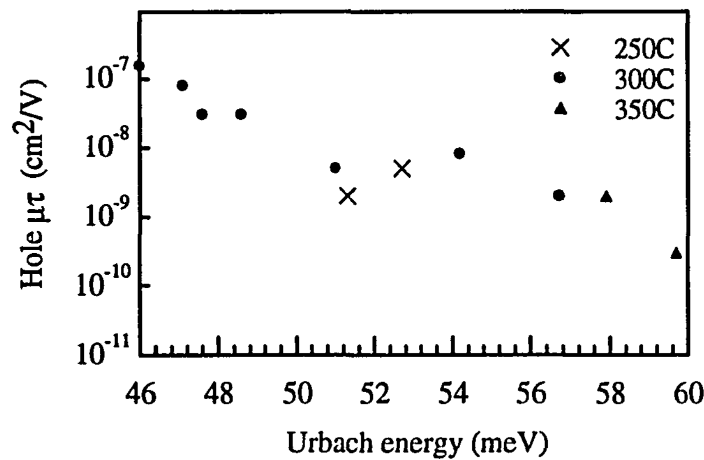

Figure 4.21. Hole mobility-lifetime product as a function of Urbach energy

Figure 4.21 also verifies that the model predicts the $\mu\tau$ product fairly accurately since the relationship shown above was found only after all of the modeling was completed. Moreover, the model does not use the Urbach energy as a parameter to fit the data. Now the Urbach energy, which is a relatively easy parameter to measure, can be used to predict the device $\mu\tau$ product.

B. Device Optimization

The final task is to optimize the device i-layer parameters for long wavelength photon absorption and carrier collection. The $\mu\tau$ product, electric field characteristics,

absorption coefficients and other parameters found from the constant bandgap devices and films are used in the model to simulate the alloyed material parameters and device conditions. For this analysis, only the i-layer is considered since the same p-layer is used for all of the devices. To determine the optimum device structure, the quantum efficiency values at long wavelengths and the device I(V) characteristics are compared.

The first step is to confirm that the idea of grading the bandgap to enhance the collection of holes actually works. There is some evidence that the change in bandgap appears primarily in the valence band, which will create a gradient in the hole potential energy.[13] Then, photogenerated holes have a better chance of reaching the p-layer.

Several devices with the grading schemes shown in Figure 4.22 were fabricated to test whether or not bandgap grading works. The devices include a constant bandgap (constant germanium content) i-layer device (a), a forward graded device that has a large germanium content near the p-i interface and then gradually decreases to pure a-Si:H at the i-n interface (b), and a reverse graded device that has a low germanium content initially, which then increases steadily toward the i-n interface (c). The names forward and reverse grading refer to the direction of the valence band gradient, which is either assisting or hindering hole drift respectively. All three of the devices have the same p- and n-layers and a buffer layer for smooth transitions between the layers.

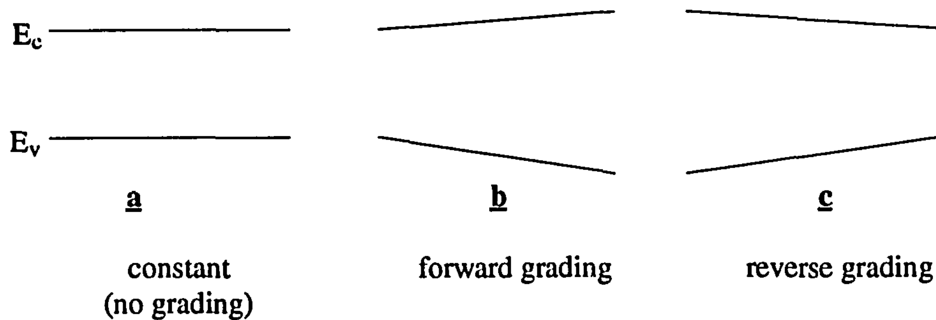

Figure 4.22. Approximate bandgap profiles in the i-layer of three test structures used to determine the effectiveness of germanium grading

The average germanium content in the three test devices is approximately the same to limit any advantages due to higher absorption coefficients or disadvantages due to increased disorder. The I(V) curves from these three devices are shown in Figure 4.23. The fill factor (and efficiency) increases from the lowest value for the reverse graded device (c), to the highest value for the forward graded structure (b). These results indicate that forward grading with germanium does enhance hole collection over the constant bandgap device, while reverse grading appears to inhibit hole collection.

Quantum efficiency (QE) ratios are an effective method for learning more about hole collection in these devices as outlined in chapter 3. When the reverse bias (-0.5 V) QE is divided by the zero-volt QE, the ratio is greater than one since the

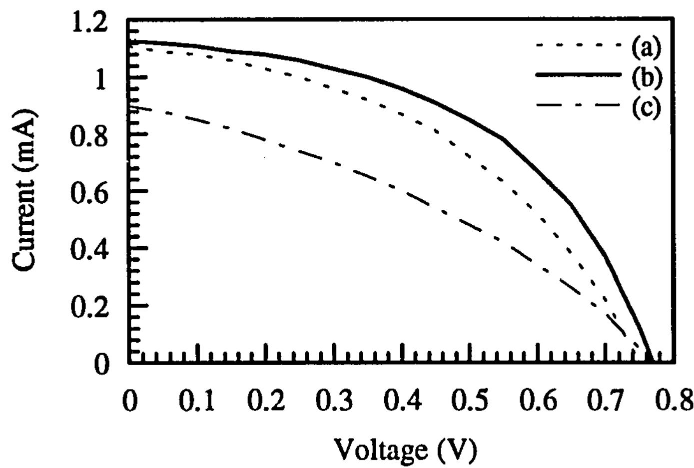

Figure 4.23. Current-voltage relationship for the reverse graded (c), constant bandgap (a), and forward graded (b) devices of Figure 4.19

reverse biasing increases the magnitude of the drift field in the device. If this ratio is nearly equal to one, then the device works well at that wavelength, since most of the holes are collected without the help of the extra electric field. When the ratio is large, it is an indication of a problem in the device. Holes generated at those wavelengths are not being collected without the excess electric field assistance.

The QE ratios for the forward and reverse graded test devices are plotted as a function of wavelength in Figure 4.24. Both of these devices have good low ratios for the high energy wavelengths (400 - 500 nm), but the ratio increases greatly for the reverse graded device at longer wavelengths. This is a clear indication that holes

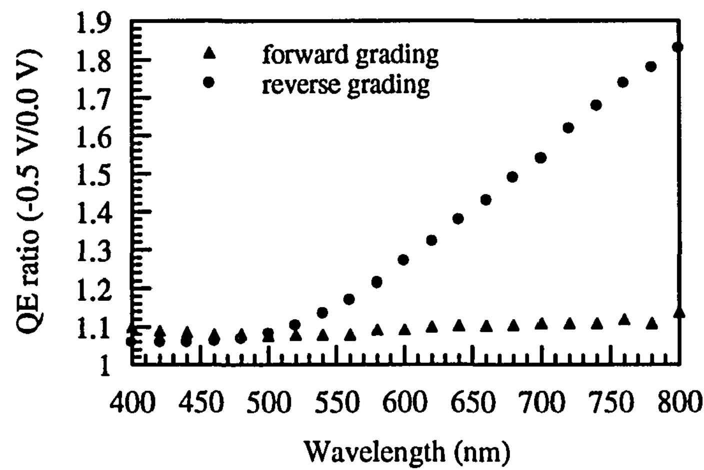

Figure 4.24. Quantum efficiency ratios for the forward and reverse graded test devices

generated away from the interface require the extra field assist provided by reverse biasing in order to be collected.

Since the only difference between these two devices is the direction of the grading, these results show that the valence and conduction band slopes play a large role in carrier collection, and that bandgap grading is an effective tool for these devices. Since hole collection is the limiting factor in the QE measurement, these results also indicate that it is primarily the valence band that changes with germanium content. With these results, device optimization can now be studied.

It was found, through modeling and fabrication, that the optimum device structure has multiple graded regions as shown in Figure 4.25. The p-i buffer layer begins with a bandgap that matches the p-type a-(Si,C):H, then drops quickly to the lowest bandgap a-(Si,Ge):H region. After the short low-bandgap region, the bandgap starts sloping gradually upward by the reduction of the germanium content until pure silicon is reached. The a-Si:H region then extends a short distance to the n-layer.

This structure maximizes the photon absorption and hole collection by creating a low bandgap region near the p-layer with a high absorption coefficient, so that a majority of the holes do not have to travel far to reach the p-layer. E_{gmin} for the device is determined by the hole transport properties of the alloy and the electric field, since all holes generated in this region and deeper in the cell must pass through this region

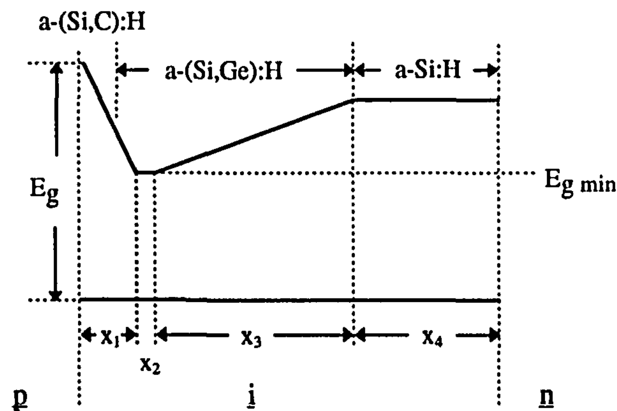

Figure 4.25. Optimized device i-layer profile determined by the model

to get to the p-layer. The germanium is graded gradually to extend the high absorption region, yet will still provide a valence band slope that enhances hole drift. The designed steepness of the slope depends on the computed magnitude of the internal electric field remaining in this region of the i-layer at forward bias operating conditions. Then, the additional a-Si:H region at the back of the i-layer further increases low energy photon absorption while using the highest quality material.

Now that the modeling is completed, optimized device fabrication can begin. The bandgap profile shown in Figure 4.25 is used as the starting point for the device fabrication. The profile will be modified to accommodate effects that are not modeled, such as the diffusion of boron from the p-layer into the i-layer. To find the optimum profile, the thickness of each region of the i-layer (x_1, x_2, x_3 and x_4 in Figure 4.25) is varied systematically, as well as the minimum bandgap E_{gmin}. To find the optimum device structure, a series of devices were fabricated with the parameters shown in Table 4.6. The values given for the thickness of each region are determined by the growth rates and deposition times.

Table 4.6 is a partial list of only those graded gap devices with the best QE and I(V) characteristics. As expected from the previous results on the films and constant bandgap devices, the best graded gap devices were deposited at 300 °C and with a -40 volt bais on the substrate.

Table 4.6. Optimized device deposition parameters

Sample #	Temp. (°C)	Eg min (eV)	x1 (Å)	x2 (Å)	x3 (Å)	x4 (Å)	Vsubstrate (V)
1/796	300	1.46	100	250	2300	2000	-40
1/797	300	1.60	120	250	2300	1550	-40
1/803	300	1.46	100	200	1860	860	-40
1/805	300	1.46	100	200	1860	1800	-40
1/807	300	1.46	--	--	--	--	-40
1/808	300	1.46	100	500	2300	500	-40
1/809	300	1.53	100	500	2300	500	-40
1/811	300	1.46	100	780	1860	500	-40
1/813	300	1.46	120	180	1620	600	-40
1/816	300	1.77	90	--	--	3600	0
1/817	250	1.61	90	300	1500	600	-40

The Tauc gap (E_{gmin}) values listed in the table are calculated from equation 4.2 using the mass flow rates from the deposition log sheets. All of the devices have the same p- and n-layers. The I(V) and QE(λ) results are used to evaluate the devices listed in the table. The device that had the highest relative long-wavelength QE is #1/803. This device had somewhat thinner x3 and x4 regions than those predicted by the model, but these are the only modifications to the parameters predicted for the optimized structure.

This result supports the other previous results, which indicated that the p-i interface fields are reduced lower than expected by the forward biasing. A thinner cell apparently is required to maintain high electric fields and hole collection. The I(V) characteristic for this device is shown in Figure 4.26, along with the I(V) characteristic of #1/807.

The I(V) curve of #1/807 is included in Figure 4.26 to show the effects of an improper i-layer grading structure. Device #1/807 has the i-layer profile shown in Figure 4.27. The minimum bandgap region is extended away from the p-i interface by a short constant-bandgap region. This was done in an attempt to boost the built-in

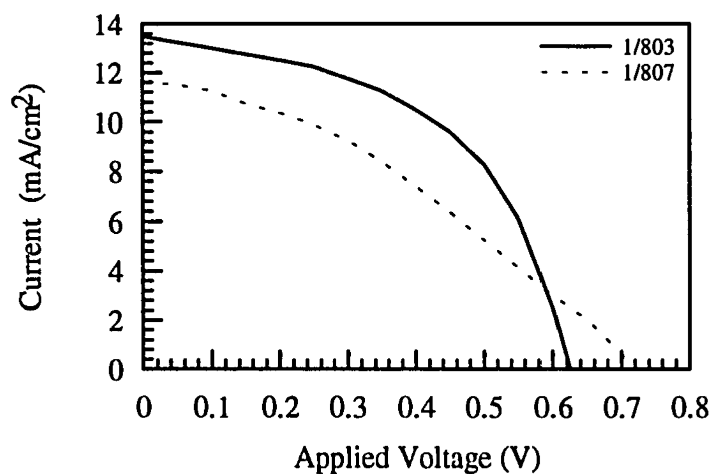

Figure 4.26. Current-voltage characteristics indicating of a proper grading scheme (1/803), and an improper grading scheme (1/807)

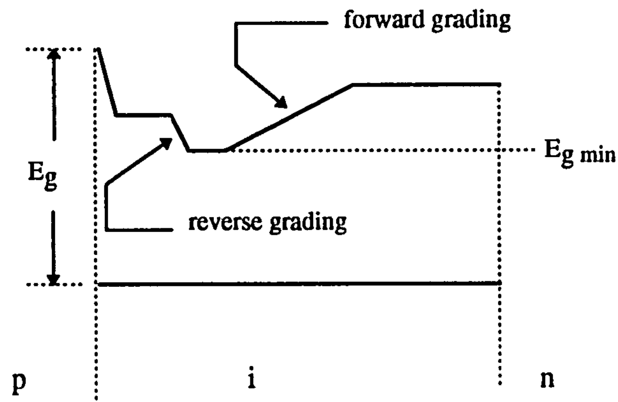

Figure 4.27. Schematic bandgap profile of device #1/807

voltage for the device. The reversed grading region shown in Figure 4.27 is required to reach the minimum bandgap.

The resulting I(V) curve in Figure 4.26 for this structure shows the effects of the reverse grading that occurred deep in the i-layer. Since the valence band is sloping in a direction that opposes the hole drift, holes generated in this region of the i-layer and beyond were much more likely to become trapped or recombine before reaching the p-layer. This is especially true when the internal electric field is reduced under forward biasing conditions. This can be seen directly in the I(V) curve in Figure 4.26. The reverse grading in the p-i interface buffer layer does not produce this effect if it is thin

enough (~100Å) since the interface field is high enough in this region to allow the holes to drift through to the p-layer.

The quantum efficiency curves for devices #1/803 and #1/816 are compared in Figure 4.28. Device #1/816 has a constant bandgap a-Si:H i-layer. Figure 4.28 shows that the low bandgap germanium and bandgap grading of sample #1/803 enhances the low energy photon absorption and carrier collection. Device #1/803 has the highest QE values at long wavelength, indicating that it has the best i-layer profile of all the cells, and would work well in a tandem cell structure.

Since the QE values are relative, with an arbitrary peak chosen at 0.9, the best indication of device quality is the ratio of a particular QE point to the peak. And,

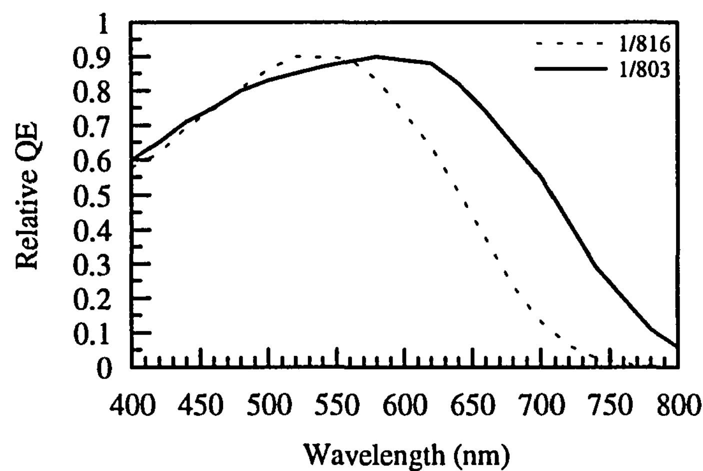

Figure 4.28. Relative quantum efficiency as a function of wavelength for a graded bandgap device (1/803) and a constant bandgap device (1/816)

since it is the long wavelength region that is of most interest, the ratios of the QE values at 680 nm and 720 nm to the peak are used here as a comparison between the different device structures. These ratios along with the I(V) curve characteristics; V_{oc}, I_{sc} and the fill factor FF, are listed in Table 4.7 for all of the devices from Table 4.6.

Since the primary goal of this project was to fabricate a device structure that is optimized for long wavelength photon collection, the efficiency of these cells by

Table 4.7. Electrical and optical properties of the graded bandgap devices

Sample #	Isc (mA/cm^2)	Voc (V)	FF (%)	QE ratio (680 nm/peak)	QE ratio (720 nm/peak)
1/796	15.00	0.67	41	0.63	0.31
1/797	15.75	0.74	48	0.49	0.19
1/803	13.00	0.65	49	0.72	0.47
1/805	10.75	0.72	40	--	--
1/807	11.75	0.72	41	--	--
1/808	12.50	0.62	53	0.50	0.27
1/809	10.25	0.64	57	0.50	0.26
1/811	11.00	0.59	48	0.42	0.21
1/813	11.00	0.69	48	0.30	0.13
1/816	11.50	0.75	51	0.26	0.07
1/817	9.50	0.76	43	0.19	0.05

themselves is not as high in the full solar spectrum as a pure a-Si:H device. The efficiency of these devices, however, can be used as another way to compare the various device structures. The initial a-(Si,Ge):H devices had an efficiency of approximately 3.2%. After all of the modeling and device optimization was completed, the efficiency has improved to 4.4%.

V. CONCLUSIONS

Hydrogenated amorphous silicon-germanium can be successfully used as a low bandgap material for tandem solar cell devices when high material quality and the proper device structure are attained. The process that was found to deposit improved quality alloyed material and a new bandgap grading scheme are described in this dissertation. Also, a new computer model used to characterize the alloyed material and to assist in device design is described.

An initial series of films were grown by PECVD to determine material quality. The photo- and dark conductivity, activation energy and subgap absorption all indicated that the films were device quality. Also, the conductivity results were more reproducible than what is usually found in the literature. To further confirm material quality, a series of constant bandgap devices with varying germanium content were fabricated. These devices also indicated that the material could be successfully used to fabricate optimized device structures down to a bandgap of about 1.5 eV.

To achieve the high material quality on a reproducible basis, the PECVD reactor is configured in a triode geometry to remove the substrate from the damaging high-energy electrons in the plasma. Also, the substrate is located out of the gas stream to limit the formation of defects in the material by powders from the plasma. The deposition conditions that produce the highest quality alloy include: low chamber

pressure (~20 mTorr), high hydrogen dilution, substrate temperatures in the 300 °C to 350 °C range and a negative substrate bias of -40V.

The films were also characterized by TEM, SEM and EDS analysis. The low temperature films appeared inhomogenous in TEM, with large regions of contrast. The homogeneity improved with increased temperature and a negative substrate bias. SEM results indicated complete substrate coverage, and EDS was used to determine the alloy composition.

The series of constant bandgap devices was used to determine the hole mobility lifetime product, Urbach energy and Tauc gap. Computer modeling is used to simulate the internal electric fields and transport properties of the p-i-n devices, in order to estimate the hole-mobility lifetime ($\mu\tau$) product. This important parameter is characterized for the first time here for a wide range of germanium concentrations.

To derive the hole $\mu\tau$ product, the model uses three parameters to fit the experimental QE(λ,V) data from the constant bandgap devices. These include the photon absorption in the p-layer, the p-i interface electric field and the $\mu\tau$ product. All of the rest of the material parameters were taken directly from experimental results. The results of the modeling correlate well with the other material parameters; again indicating that the highest quality material was deposited at 300 °C, and with the other deposition conditions listed above.

After the material quality modeling was completed on the constant bandgap devices, a relationship between the hole $\mu\tau$ product and a parameter that could be easily measured was searched for. There did not appear to be a direct relationship between the germanium content and $\mu\tau$, which is not surprising since the other conditions during deposition also affect $\mu\tau$. A clear exponential relationship between $\mu\tau$ and the Urbach energy was found. This relationship is probably a direct consequence of the dispersive transport of holes as they 'hop' into and out of the valence band tail states. Also, the Urbach energy and $\mu\tau$ should be affected by the germanium content and deposition conditions in the same way, since both parameters are affected by the defect density. This is a very useful result since now the transport parameters can be estimated by simply using this relationship and the relatively easy Urbach energy measurement.

Once the material quality and reproducibility were well established, device optimization was completed. First, the concept of bandgap grading was tested to confirm that it would provide beneficial results to the operation of the cell. Constant bandgap, and forward and reverse graded test cells were fabricated. The forward graded cell had the best I(V) and QE characteristics, indicating that the hole collection was enhanced by the valence band gradient.

Then, the computer model was used to guide the design of the initial optimized device structures. The goal was to optimize the cell for long wavelength photon

collection rather than to achieve the highest efficiency in the full solar spectrum. A multiple-graded gap cell with a minimum bandgap of about 1.46 eV was found to improve the long wavelength photon absorption and carrier collection over constant bandgap and the simple forward graded cells. A p-i interface buffer layer was required to limit boron diffusion into the i-layer and to limit the effects of hole trapping at the interface. The improvement in long wavelength photon collection for low bandgap cells from the start of this project to the conclusion was approximately 20%. This silicon-germanium cell can be effectively used to increase the efficiency of a tandem cell structure.

REFERENCES

1. Carlson, D.E., and Wronski, C.R., "Amorphous silicon solar cell," Applied Physics Letters, vol. 28, no.11, p. 671, 1976.

2. Chittick, R.C., Alexander, J.H., and Sterling, H.F., Journal of the Electrochemical Society, vol. 116, no. 77, p. 93, 1969.

3. Spear, W.E., and Lecomber, P.G., Journal of Non-Crystalline Solids, vol. 8-10, p. 727, 1972.

4. Spear, W.E., and Lecomber, P.G., Solid State Communications, vol. 17, p. 1193, 1975.

5. Staebler, D.L., and Wronski, C.R., "Reversible conductivity changes in discharge-produced amorphous Si," Applied Physics Letters, vol. 31, no.4, p. 292, Aug. 1977.

6. Arya, R.R., Yang, L., Bennett, M., et al., "Status, Progress and challenges in high performance, stable amorphous silicon alloy based triple junction modules," Proceedings of 23rd. IEEE PVSC, p. 790, 1993.

7. Dalal, V.L., Baldwin, G., and Garikepati, P., "Improvements in stability of a-silicon solar cells through the use of bandgap grading," Proceedings of 23rd. IEEE PVSC, p. 816, 1993.

8. Madan, A., and Shaw, M.P., The Physics and Application of Amorphous Semiconductors, Academic Press, San Diego, 1988.

9. Mott, N.F., and Davis, E.A., Electronic Processes in Non-Crystalline Materials, Clarendon Press, Oxford, 1979.

10. Street, R.A., Hydrogenated Amorphous Silicon, Cambridge University Press, Cambridge, U.K., 1991.

11. Properties of Amorphous Silicon, EMIS Datareview Series No. 1, ed. Fritzsche, H., ISPEC, New York, 1989.

12. Zachariasen, W.H., Journal of the American Chemical Society, vol. 54, p. 3841, 1932.

13. Mackenzie, K.D., Eggert, J.R., Leopold, D.J., Li, Y.M., Lin, S., and Paul, W., "Structural, electrical, and optical properties of a-(Si,Ge):H and an inferred band structure," Physical Review B, vol. 31, no. 4, p. 2198, Feb. 1985.

14. Street, R.A., "Model for the growth of plasma deposited a-Si:H and related materials," Journal of Non-Crystalline Solids, vol. 137-138 p. 645 1991.

15. Baldwin, G., "Analytical and numerical modeling of a graded band gap amorphous silicon based p-i-n solar cell," Master's Thesis, Iowa State University, 1991.

16. Smith, R.A., Semiconductors, p. 184-8, Cambridge University Press, New York, 1978.

17. Guha, S., Yang, J., Pawlikiewics, A.H., Glatfelter, T., Ross, R., and Ovshinsky, S.R., "Band gap profiling for improving the efficiency of amorphous silicon-alloy solar cells.", Applied Physics Letters, vol. 54, no. 23, p. 2330, 1989.

18. Baldwin, G., Dalal, V., and Han, K., "Deposition of high quality a-(Si,Ge):H films and novel graded gap devices using rf triode glow discharge deposition," Proceedings of 23rd. IEEE PVSC, p. 1037, 1993.

19. Paul, W., Street, R.A., and Wagner, S., "Hydrogenated amorphous semiconductors," Journal of Electronic Materials, vol. 22, no. 1, p. 39, 1993.

20. Hack, M., and Shur, M., "Physics of amorphous silicon alloy p-i-n solar cells," Journal of Applied Physics, vol. 58, no. 2, p. 997, 1985.

21. Tsuda, S., Takahama, T., Hishikawa, Y., et al., "A-Si technologies for high efficiency solar cells," to be published in Journal of Non-Crystalline Solids, 1994.

22. Mackenzie, K.D., Burnett, J.H., Eggert, J.R., Li, Y.M., and Paul, W., "Comparison of the structural, electrical, and optical properties of amorphous silicon-germanium alloys produced from hydrides and fluorides," Physical Review B, vol. 38, no. 9, p. 6120, Sept. 1988.

23. Pankove, J., Optical processes in Semiconductors, Dover Publications, New York, 1971.

24. Perrin, J., "Plasma and surface reactions during a-Si:H film growth," Journal of Non-Crystalline Solids, vol. 137-138, p. 639, 1991.

25. Schubert, M., Weller, H., Eberhardt, K., and Bauer, G., "Structural properties of a-$Si_{1-x}Ge_x$:H," Journal of Non-Crystalline Solids, vol. 114, p. 528, 1989.

26. Vanderhagen, R., Longeaud, C., "Influence of the incorporation of germanium on the tail states in amorphous semiconductors," Journal of Non-Crystalline Solids, vol. 114, p. 540, 1989.

27. Winer, K., "Defect pool model of defect formation in a-Si:H," Journal of Non-Crystalline Solids, vol. 137-138, p. 157, 1991.

28. Balberg, I., and Lubianiker, Y., "Evidence for the defect-pool model from induced recombination level shifts in undoped a-Si:H," Physical Review B, vol. 48, no. 12, p. 8709, Sept. 1993.

29. Aljishi, S., Cohen, J.D., Jin, S., and Ley, L., "Band tails and thermal disorder in doped and undoped hydrogenated amorphous silicon and silicon-germanium alloys," Materials Research Society Symposium Proceedings, vol. 192, p. 157, 1990.

30. Paul, W., "Structural, optical and photoelectronic properties of improved PECVD a-Ge:H," Journal of Non-Crystalline Solids, vol. 137-138, p. 803, 1991.

31. Fortmann, C., Dawson, R., Gunes, M., and Wronski, C., "Amorphous silicon dispersive transport considerations for analysis of films and solar cells," to be published in Journal of Non-Crystalline Solids, 1994.

32. Pierz, K., Fuhs, W., and Mell, H., "Correlation between defect density and Fermi level position in a-Si:H," Journal of Non-Crystalline Solids, vol. 114, p. 651, 1989.

33. Orenstein, J., Kastner, M., and Vaninov, V., "Transient photoconductivity and photo-induced optical absorption in amorphous semiconductors," Philosophical Magazine B, vol. 46, no. 1, p. 23, 1982.

34. Fortmann, C., "Prospects of a-SiGe:H alloys for solar cell application," Materials Research Society Symposium Proceedings, vol. 192, p. 27, 1990.

35. Unold, T., and Cohen, J.D., "Density of states and carrier dynamics in amorphous silicon germanium alloys and amorphous germanium," Journal of Non-Crystalline Solids, vol. 137-138, p. 809, 1991.

ACKNOWLEDGMENTS

I would like to take this opportunity to thank those who were integral to the completion of this project. I am greatly indebted to my major professor, Dr. Vikram Dalal, for his guidance and support throughout my graduate studies. Also, I would not have gotten this far without the support of my wife Laura, who has set aside her own goals while I have worked on mine. The financial support provided by the private donations of William Catron has also contributed greatly to this project.

Further financial support came from the Department of Education and the Iowa Electric Power Corporation. I would like to thank Dr. Stanley Burns, Dr. Scott Chumbley, Dr. Howard Shanks and Dr. Gary Tuttle for serving on my graduate committee and providing useful advice. Others who provided technical assistance include Dr. W. Straszheim, Dr. F. Laabs and Keqin Han. Help with the manuscript was provided by Scott DeBoer and Dr. Ralph Knox.

Finally, I would like to thank my parents for their support and those who helped me by providing technical assistance as well as friendship; Er-Xuan Ping, Scott DeBoer, Sanjiv Kaushal, Russ Bruhn, Behnam Moradi, Mark Leonard, and Dr. Ralph Knox.

APPENDIX: CONSTANT BANDGAP DEVICE PARAMETERS

Table A.1. Constant bandgap device deposition parameters and characteristics

Sample #	Pressure (mTorr)	Temp (°C)	i-layer Time (min.)	Eμ (meV)	Eg (eV)	Gas Flow Rates: 100% SiH_4 (sccm)	10% GeH_4 (sccm)	100% H_2 (sccm)
1/536	30	300	90	47.1	1.68	6	4	60
1/545	25	300	90	47.8	1.70	8	4	50
1/574	24	300	60	47.4	1.71	8	2	50
1/577	26	300	60	47.6	1.64	8	6	50
1/626	26	300	50	48.6	1.62	6	8	50
1/630	32	300	120	54.2	1.59	4	8	60
1/632	20	300	60	51.2	1.57	3	8	40
1/635	20	300	56	48.6	1.61	8	8	40
1/638	17	250	135	51.3	1.67	2	4	40
1/639	18	250	100	52.7	1.57	2	8	40
1/640	18	250	50	54.1	1.59	2	8	40
1/641	18	300	50	51.0	1.56	2	8	40
1/642	20	300	60	57.1	1.38	2	12	40
1/655	16	300	120	46.0	1.77	4	0	0
1/676	20	350	45	59.7	1.43	2	12	40
1/677	26	350	45	71.8	1.21	2	24	40
1/681	22	350	45	57.9	1.32	2	16	40
1/682	22	300	45	56.7	1.41	2	16	40